VOLUME 8 NUMBER 1 2017 ISSN 2218-7987

International Journal of Mathematics and Physics

Al-Farabi Kazakh National University

International Journal of Mathematics and Physics is publishing two numbers in a year by al-Farabi Kazakh National University, al-Farabi ave., 71, 050040, Almaty, the Republic of Kazakhstan
website: http://ijmph.kaznu.kz/

Any inquiry for subscriptions should be send to:
Prof. Tlekkabul Ramazanov, al-Farabi Kazakh National University
al-Farabi ave., 71, 050040, Almaty, the Republic of Kazakhstan
e-mail: Tlekkabul.Ramazanov@kaznu.kz

 Printed in Kazakhstan

Editorial

The most significant scientific achievements are attained through joint efforts of different sciences, mathematics and physics are among them. Therefore publication of the Journal, which shows results of current investigations in the field of mathematics and physics, will allow wider exhibition of scientific problems, tasks and discoveries.

One of the basic goals of the Journal is to promote extensive exchange of information between scientists from all over the world. We propose publishing service for original papers and materials of Mathematical and Physical Conferences (by selection) held in different countries and in the Republic of Kazakhstan.

Creation of the special International Journal of Mathematics and Physics is of great importance because a vast amount of scientists are willing to publish their articles and it will help to widen the geography of future dissemination. We will also be glad to publish papers of scientists from all the continents.

The Journal will publish experimental and theoretical investigations on Mathematics, Physical Technology and Physics. Among the subject emphasized are modern problems of Calculus Mathematics, Algebra and Mathematical Analysis, Differential Equations and Mechanics, Informatics and Mathematical Modeling, Calculus of Approximations and Program Systems, Astronomy and Space Research, Theoretical Physics and Plasma Physics, Chemical Physics and Radio Physics, Thermophysics, Nuclear Physics and Nanotechnology.

The Journal is issued on the base of al-Farabi Kazakh National University. Leading scientists from different countries of the world agreed to join the Editorial Board of the Journal.

The Journal will be published two times a year by al-Farabi Kazakh National University. We hope to receive papers from many laboratories which are interested in applications of the scientific principles of mathematics and physics and are carrying out researches on such subjects as production of new materials or technological problems.

UDC 517.968.2

[1*]Aisagaliev S., [1]Zhunussova Zh., [2]Akca H.

[1]Al-Farabi Kazakh National University, Almaty, Kazakhstan
[2]Abu-Dhabi University, Abu-Dhabi, UAE
[*]e-mail: Zhanat.Zhunusova@kaznu.kz

Solvability of a two-point boundary value problem with phase and integral constraints

Abstract. New mathematical techniques for considering the complex boundary value problems to solve topical problems of natural sciences, technology, economy and ecology etc. are needed. Mathematical models of nuclear and chemical reactors management processes, control of electric power and robotic systems, economic management and others are complex boundary value problems of ordinary differential equations. Boundary value problems are called complex if besides the boundary conditions there exist the phase constraints and integral constraints on the phase coordinates of the system. The main objectives are: the necessary and sufficient conditions for the existence of solutions of boundary value problems and the methods of construction of complex solutions of boundary value problems. The aim of the work is an attempt to create a unified theory of the study of solvability of boundary value problems and the construction of a general method for solving them, based on the use of modern computer technology. The work is devoted to solving the problems of boundary value problems of nonlinear systems of ordinary differential equations. We consider the boundary value problem with boundary conditions of the given convex closed sets. The necessary and sufficient conditions for existence of a solution of the problem and construction its solution are obtained. The basis of the proposed method for solving of the boundary value problem is a possibility to reduce to a class of linear Fredholm integral equation of the first kind [1]-[9]. Necessary and sufficient condition for existence of a solution of integral equation is proved. Fredholm integral equation of the first kind belongs to the insufficiently explored problems in mathematics [11]-[22].

Key words: integral equation, solvability, construction of a solution, extreme problem, functional gradient, minimizing sequence.

Introduction

We consider and find necessary and sufficient conditions for existence of a solution of the boundary value problem

$$\dot{x} = A(t)x + \mu(t),\ t \in I = [t_0, t_1], \qquad (1)$$

$$(x(t_0) = x_0, x(t_1) = x_1) \in S \subset R^{2n}, \qquad (2)$$

at phase constraints

$$x(t) \in G(t);$$
$$G(t) = \{x \in R^n / \ \omega(t) \le L(t)x \le \phi(t),$$
$$t \in I\},$$

integral constraints

$$g_j(x) \le c_j, \quad j = \overline{1, m_1},$$
$$g_j(x) = c_j, \quad j = \overline{m_1 + 1, m_2},$$

$$g_j(x) = \int_{t_0}^{t_1} < a_j(t), x > dt, \qquad j = \overline{1, m_2},$$

here $A(t)$, $L(t)$ are matrixes of $n \times n$, $s \times n$ order, accordingly, with piece-wise continuous elements, S is the given closed set, $\omega(t)$, $\varphi(t)$, $t \in I$ are the prescribed continuous vector functions $s \times 1$, $a_j(t)$, $j = \overline{1, m_2}$ are the given piece-wise continuous vector functions of $n \times 1$ order, c_j, $j = \overline{1, m_2}$ are unknown constants, t_0, t_1 are the fixed time moments, $\mu(t) = (\mu_1(t), ..., \mu_n(t))$ is the prescribed piece-wise continuous function, $< \cdot, \cdot >$ is a scalar production. We construct a solution of the linear system (1) with boundary conditions (2).

We represent the matrix $A(t)$ of $n \times n$ order with piecewise continuous elements as the sum $A(t) = A_1(t) + B(t)$, $t \in I$, that the matrix

$$W(t_0,t_1)=\int_{t_0}^{t_1}\Phi(t_0,t)B(t)B^*(t)\Phi^*(t_0,t)dt$$

of $n\times n$ order be positive defined, where $\Phi(t,\tau)=\theta(t)\theta^{-1}(\tau)$, $\theta(t)$ is a fundamental matrix solutions of the linear homogeneous system $\dot{\xi}=A_1(t)\xi$. We note, that the matrix $\theta(t)$ is a solution of the equation $\dot{\theta}(t)=A_1(t)\theta(t)$, $\theta(t_0)=I_n$, where I_n is an unique matrix of $n\times n$ order. There are many options for representation the matrix $A(t)$ as the sum $A(t)=A_1(t)+B(t)$, $t\in I$:

1. The matrix $A_1(t)$ can be chosen as a constant matrix A_1 of $n\times n$ order. In this case $\theta(t)=e^{A_1t}$, $t\in I$;

2. The matrix $B(t)$ is chosen in the form $B(t)=B_1(t)P$, where $B_1(t)$ is the matrix of $n\times m$ order, P is a constant matrix of $m\times n$ order, moreover $P=\left(I_m,0_{m,n-m}\right)$, where I_m is an unique matrix of $m\times m$ order, $0_{m,n-m}$ is a rectangular matrix of $m\times(n-m)$ order with zero elements.

Since the matrix $A(t)=A_1(t)+B(t)$, $t\in I$, that equation (1) is written as

$$\dot{x}=A_1(t)x+B(t)x+\mu(t),\ t\in I=[t_0,t_1]. \quad (3)$$

In the case of a choice $B(t)=B_1(t)P$ the equation (3) has the form

$$\dot{x}=A_1(t)x+B_1(t)Px+\mu(t),\ t\in I, \quad (4)$$

where $B_1(t)$ is a matrix of $n\times m$ order, Px is the vector function $m\times 1$. If $m=n$, then $P=I_n$, $B(t)=B_1(t)$, $t\in I$. Without loss of generality, further we believe, that equation (4) is represented in the form (4), the matrix

$$W_1(t_0,t_1)=\int_{t_0}^{t_1}\Phi(t_0,t)B_1(t)B_1^*(t)\Phi^*(t_0,t)dt. \quad (5)$$

In addition to (4), we consider the linear control system of the form

$$\dot{y}=A_1(t)y+B_1(t)u(t)+\mu(t),\ t\in I, \quad (6)$$

$$\left(y(t_0)=x_0,y(t_1)=x_1\right)\in S\subset R^{2n}, \quad (7)$$

$$u(\cdot)\in L_2(I,R^m). \quad (8)$$

We note, that if $u(t)=Px(t)$, $t\in I$, then the system (6)-(8) coincides with the origin system (1), (2).

Solution of a linear control system

We use the following theorems 1 and 2. The theorems are proved in our previous works [1]-[9].

A solution of the boundary value problem relates to properties of the solutions of the following integral equation

$$Ku=\int_{t_0}^{t_1}K(t_0,t)u(t)dt=a,\ t\in I=[t_0,t_1], \quad (2.1)$$

where $K(t_0,t)=\left\|K_{ij}(t_0,t)\right\|$, $i=\overline{1,n}$, $j=\overline{1,m}$ is the known matrix of $n\times m$ order with piecewise continuous by t elements at fixed t_0, t_1, $u(\cdot)\in L_2(I,R^m)$ is the origin function, operator $K:L_2(I,R^m)\to R^n$, $a\in R^n$ is prescribed vector.

Theorem 1. *Integral equation (2.1) at any fixed $a\in R^n$ has a solution if and only if the matrix*

$$C(t_0,t_1)=\int_{t_0}^{t_1}K(t_0,t)K^*(t_0,t)dt \quad (2.2)$$

of $n\times n$ order is positive defined, where $(*)$ is a transposition sign, $t_1>t_0$.

Theorem 2. *Let $C(t_0,t_1)>0$ be a matrix. Then the general solution of integral equation (2.1) has the form*

$$u(t)=K^*(t_0,t)C^{-1}(t_0,t)a+v(t)-$$
$$-K^*(t_0,t)C^{-1}(t_0,t_1)\int_{t_0}^{t_1}K(t_0,t)v(t)dt, \quad (2.3)$$

where $t\in I$, $v(\cdot)\in L_2(I,R^m)$ is an arbitrary function, $a\in R^n$ is any vector.

Theorem 3. *Let the matrix* $W_1(t_0,t_1)$ *of* $n\times n$ *order be positive defined. Then control* $u(\cdot)\in L_2(I,R^m)$ *transfers the trajectory of system (6) from any initial point* $y(t_0)=x_0\in R^n$ *to any finite state* $y(t_1)=x_1\in R^n$ *if and only if*

$$u(t)\in U=\{u(\cdot)\in L_2(I,R^m)/\,u(t)=v(t)+\lambda_1(t,x_0,x_1)+N_1(t)z(t_1,v),t\in I,\forall v,v(\cdot)\in L_2(I,R^m)\},\quad(9)$$

where

$$\lambda_1(t,x_0,x_1)=B_1^*(t)\Phi^*(t_0,t)W_1^{-1}(t_0,t_1)a,$$

$$a=\Phi(t_0,t_1)x_1-x_0-\int_{t_0}^{t_1}\Phi(t_0,t)\mu(t)dt,$$

$$N_1(t)=-B_1^*(t)\Phi^*(t_0,t)W_1^{-1}(t_0,t_1)\Phi(t_0,t_1).$$

Function $z(t,v)$, $t\in I$ *is a solution of the differential equation*

$$\dot z=A_1(t)z+B_1(t)v(t),\ z(t_0)=0,\quad v(\cdot)\in L_2(I,R^m).\quad(10)$$

Solution of differential equation (6) corresponding to control $u(t)\in U$ *is defined by formula*

$$y(t)=z(t,v)+\lambda_2(t,x_0,x_1)+N_2(t)z(t_1,v),\quad(11)$$

where $t\in I$,

$$\lambda_2(t,x_0,x_1)=\Phi(t,t_0)W_1(t,t_1)W_1^{-1}(t_0,t_1)x_0+\Phi(t,t_0)W_1(t_0,t)W_1^{-1}(t_0,t_1)\Phi(t_0,t_1)x_1+\int_{t_0}^{t}\Phi(t,\tau)\mu(\tau)d\tau-\Phi(t,t_0)W_1(t_0,t)W_1^{-1}(t_0,t_1)\int_{t_0}^{t_1}\Phi(t_0,t)\mu(t)dt$$

$$N_2(t)=-\Phi(t,t_0)W_1(t_0,t)W_1^{-1}(t_0,t_1)\Phi(t_0,t_1),$$

$$W(t_0,t)=\int_{t_0}^{t}\Phi(t_0,\tau)B_1(\tau)B_1^*(\tau)\Phi^*(t_0,\tau)d\tau,$$

$$W(t,t_1)=W(t_0,t_1)-W(t_0,t).$$

Proof. Solution of the system (6) has the form

$$y(t)=\Phi(t,t_0)x_0+\int_{t_0}^{t}\Phi(t,\tau)B_1(\tau)u(\tau)d\tau+\int_{t_0}^{t}\Phi(t,\tau)\mu(\tau)d\tau,\quad t\in I,$$

Then the control which transfers the trajectory of system (6) from initial state $x_0\in R^n$ to the state $x_1\in R^n$ is defined by condition

$$y(t_1)=x_1=\Phi(t_1,t_0)x_0+\int_{t_0}^{t_1}\Phi(t_1,t)B_1(t)u(t)dt+\int_{t_0}^{t_1}\Phi(t_1,t)\mu(t)dt.$$

This implies

$$\int_{t_0}^{t_1}\Phi(t_1,t)B_1(t)u(t)dt=x_1-\Phi(t_1,t_0)x_0-\int_{t_0}^{t_1}\Phi(t_1,t)\mu(t)dt.\quad(12)$$

Since $\Phi(t_1,t)=\Phi(t_1,t_0)\Phi(t_0,t)$, $\Phi^{-1}(t_1,t_0)=\Phi(t_0,t_1)$, that expression (12) is written in the form

$$\int_{t_0}^{t_1}\Phi(t_0,t)B_1(t)u(t)dt+\Phi(t_0,t_1)x_1-x_0-\int_{t_0}^{t_1}\Phi(t_0,t)\mu(t)dt=a.\quad(13)$$

Thus, the origin equation $u(\cdot)\in L_2(I,R^m)$ is a solution of the integral equation (13). Integral equation (13) can be represented as

$$Ku=\int_{t_0}^{t_1}K(t_0,t)u(t)dt=a,$$

$$K(t_0,t)=\Phi(t_0,t)B_1(t),\ t\in I.$$

As it follows from theorem 1, integral equation (13) has a solution if and only if the matrix

$$C(t_0,t_1)=\int_{t_0}^{t_1}K(t_0,t)K^*(t_0,t)dt=$$

$$=\int_{t_0}^{t_1}\Phi(t_0,t)B_1(t)B_1^*(t)\Phi^*(t_0,t)dt=W_1(t_0,t_1)$$

of $n\times n$ order is positive defined. Consequently, the set $U\neq\varnothing$, $\varnothing$ is an empty set if and only if $W_1(t_0,t_1)>0$. It means, that the system (6)-(9) is controlled.

From theorem 2 it follows, that the general solution of the integral equation (13) has the form

$$u(t)=K^*(t_0,t)C^{-1}(t_0,t_1)a+v(t)-$$

$$-K^*(t_0,t)C^{-1}(t_0,t_1)\int_{t_0}^{t_1}K(t_0,t)v(t)dt\,,$$

where

$$K(t_0,t)=\Phi(t_0,t)B_1(t),$$

$$C(t_0,t_1)=W_1(t_0,t_1).$$

This implies

$$u(t)=B_1^*(t)\Phi^*(t_0,t)W_1^{-1}(t_0,t_1)a+v(t)-B_1^*(t)\Phi^*(t_0,t)\times W^{-1}(t_0,t_1)\int_{t_0}^{t_1}\Phi(t_0,t)B_1(t)v(t)dt,\ t\in I,\qquad(14)$$

where $v(\cdot)\in L_2(I,R^m)$ is any function. We note, that solution of differential equation (10) has the form

$$z(t)=z(t,v)=\Phi(t,t_0)z(t_0)+$$

$$+\int_{t_0}^{t}\Phi(t,\tau)B_1(\tau)v(\tau)d\tau=\quad,\qquad(15)$$

$$=\int_{t_0}^{t}\Phi(t,\tau)B_1(\tau)v(\tau)d\tau$$

where $z(t_0)=0$. Consequently,

$$z(t_1)=z(t_1,v)=\int_{t_0}^{t_1}\Phi(t_1,t)B_1(t)v(t)dt=$$

$$=\Phi(t_1,t_0)\int_{t_0}^{t_1}\Phi(t_0,t)B_1(t)v(t)dt.\qquad(16)$$

From (14)-(16) it follows, that the origin control $u(t)=v(t)+\lambda_1(t,x_0,x_1)+N_1(t)z(t_1,v)$, $t\in I$, $\forall v$, $v(\cdot)\in L_2(I,R^m)$.

This implies proposition of the theorem that $u(t)\in U$. Finally, inclusion (9) is proved.

Let $u(t)\in U$. Then solution of differential equation (6) has the form

$$y(t)=\Phi(t,t_0)x_0+\int_{t_0}^{t}\Phi(t,\tau)B_1(\tau)[v(\tau)+\lambda_1(\tau,x_0,x_1)+N_1(\tau)z(t_1,v)]d\tau+$$

$$+\int_{t_0}^{t}\Phi(t,\tau)\mu(\tau)d\tau=\int_{t_0}^{t}\Phi(t,\tau)B_1(\tau)v(\tau)d\tau+\Phi(t,t_0)x_0+\int_{t_0}^{t}\Phi(t,\tau)B_1(\tau)\times$$

$$\times B_1^*(\tau)\Phi^*(t_0,\tau)d\tau W_1^{-1}(t_0,t_1)[\Phi(t_0,t_1)x_1-x_0-\int_{t_0}^{t_1}\Phi(t_0,t)\mu(t)dt]-$$

$$-\int_{t_0}^{t}\Phi(t,\tau)B_1(\tau)B_1^*(\tau)\Phi^*(t_0,\tau)d\tau W_1^{-1}(t_0,t_1)\Phi(t_0,t_1)z(t_1,v)=z(t,v)+$$

$$+\lambda_2(t,x_0,x_1)+N_2(t)z(t_1,v),\ t\in I.$$

This implies representation of solution of the system (6) in the form (11). Theorem is proved.

It is easy to make sure in that

$$y(t_0)=z(t_0,v)+\lambda_2(t_0,x_0,x_1)+N_2(t_0)z(t_1,v)=x_0,$$

$$y(t_1)=z(t_1,v)+\lambda_2(t_1,x_0,x_1)+N_2(t_1)z(t_1,v)=x_1.$$

Since proposition of the theorem is valid for any $x_0 \in R^n$, $x_1 \in R^n$, that it is valid, when $(x_0, x_1) \in S \subset R^{2n}$.

Lemma 1. *Let $W_1(t_0,t_1) > 0$ be a matrix. Then the boundary value problem (1), (2) is equivalent to the following problem:*

$$\begin{gathered} v(t) + T_1(t)x_0 + T_2(t)x_1 + \overline{\mu}(t) + \\ + N_1(t)z(t_1, v) = Py(t) \\ t \in I \end{gathered}, \quad (17)$$

$$\dot{z} = A_1(t)z + B_1(t)v(t),\ z(t_0) = 0, \quad t \in I, \quad v(\cdot) \in L_2(I, R^m), \quad (18)$$

$$(x_0, x_1) \in S, \quad (19)$$

where

$$T_1(t) = -B_1^*(t)\Phi^*(t_0,t)W_1^{-1}(t_0,t_1),$$

$$T_2(t) = B_1^*(t)\Phi^*(t_0,t)W^{-1}(t_0,t_1)\Phi(t_0,t_1),$$

$$\overline{\mu}(t) = -B_1^*(t)\Phi^*(t_0,t)W_1^{-1}(t_0,t_1)\int_{t_0}^{t_1}\Phi(t_0,t)\mu(t)dt,$$

$$\begin{gathered} y(t) = z(t,v) + C_1(t)x_0 + C_2(t)x_1 + \\ + f(t) + N_2(t)z(t_1,v) \end{gathered}, \quad (20)$$

$$C_1(t) = \Phi(t,t_0)W_1(t,t_1)W_1^{-1}(t_0,t_1),$$

$$C_2(t) = \Phi(t,t_0)W_1(t_0,t)W_1^{-1}(t_0,t_1)\Phi(t_0,t_1),$$

$$f(t) = \int_{t_0}^{t}\Phi(t,\tau)\mu(\tau)d\tau -$$

$$-\Phi(t,t_0)W_1(t_0,t)W_1^{-1}(t_0,t_1)\int_{t_0}^{t_1}\Phi(t_0,t)\mu(t)dt.$$

Proof of the lemma follows from theorem 3 and the equality $y(t) = x(t)$, $t \in I$, at $u(t) \in U$, $u(t) = Py(t)$, $t \in I$. It is easy to make sure that expressions (17) – (19) are equivalent to the expressions (1), (2), at $W_1(t_0,t_1) > 0$.

We consider the optimal control problem: minimize the functional

$$I(v, x_0, x_1) = \int_{t_0}^{t_1}\left|v(t) + T_1(t)x_0 + T_2(t)x_1 + \overline{\mu}(t) + N_1(t)z(t_1,v) - Py(t)\right|^2 dt \to \inf, \quad (21)$$

at conditions

$$\dot{z} = A_1(t)z + B_1(t)v(t),\ z(t_0) = 0,\ t \in I, \quad (22)$$

$$v(\cdot) \in L_2(I, R^m),\ (x_0, x_1) \in S, \quad (23)$$

where $y(t) = y(t, v, x_0, x_1)$, $t \in I$ is defined by formula (23).

We note, that:

1. Functional $I(v, x_0, x_1) \geq 0$. Consequently, functional $I(v, x_0, x_1)$ is bounded below on the set $X = L_2(I, R^m) \times S$, where $(v, x_0, x_1) \in X \subset H$, $H = L_2(I, R^m) \times R^{2n}$.

2. If $I(v_*, x_{0*}, x_{1*}) = 0$, where $(v_*, x_{0*}, x_{1*}) \in X$, is a solution of the optimization problem (21)-(23), then

$$\begin{gathered} x_*(t) = y_*(t, v_*, x_{0*}, x_{1*}) = z(t, v_*) + C_1(t)x_{0*} + \\ + C_2(t)x_{1*} + f(t) + N_2(t)z(t_1, v_*), \end{gathered}$$

$t \in I$ is solution of the boundary value problem (1), (2).

Necessary and sufficient condition for existence of a solution of the two-point boundary value problem

Theorem 4. *Let $W_1(t_0,t_1) > 0$ be a matrix. In order to the boundary value problem (1), (2) has a solution, necessary and sufficiently, that the value $I(v_*, x_{0*}, x_{1*}) = 0$, where $(v_*, x_{0*}, x_{1*}) \in X$ is a solution of the optimization problem (21) – (23).*

Proof. *Necessity.* Let boundary value problem (1), (2) has a solution. We show, that the value

$I(v_*, x_{0*}, x_{1*}) = 0$. Let $x(t; t_0, x_{0*}, x_{1*})$, $t \in I$, $(x_{0*}, x_{1*}) \in S$ be a solution of differential equation (1). As it follows from lemma 1, boundary value problem (1), (2) is equivalent to the problem (17) – (19). Hence,

$$\left.\begin{array}{c} v_*(t) + T_1(t)x_{0*} + T_2(t)x_{1*} + \\ + \bar{\mu}(t) + N_1(t)z(t_1, v_*) = Py_*(t) \\ t \in I, \end{array}\right. \quad (24)$$

$$\dot{z}(t, v_*) = A_1(t)z(t, v_*) + B_1(t)v_*(t),\ z(t_0) = 0,$$

$$t \in I,\ v_*(\cdot) \in L_2(I, R^m), \quad (25)$$

$$\left.\begin{array}{c} y_*(t) = z(t, v_*) + C_1(t)x_{0*} + C_2(t)x_{1*} + \\ + f(t) + N_2(t)z(t_1, v_*) \\ t \in I \end{array}\right.,$$

where $(x_{0*}, x_{1*}) \in S$, $u(t) \in U$, $u(t) = Py_*(t)$, $t \in I$, $y_*(t) = x(t; t_0, x_{0*}, x_{1*})$, $t \in I$.

Then

$$I(v_*, x_{0*}, x_{1*}) = \int_{t_0}^{t_1} \left| v_*(t) + T_1(t)x_{0*} + T_2(t)x_{1*} + \bar{\mu}(t) + N_1(t)z(t_1, v_*) - Py_*(t) \right|^2 dt = 0,$$

by identities (24), (25). Necessity is proved.

Sufficiency. Let $I(v_*, x_{0*}, x_{1*}) = 0$ be the value. We show, that boundary value problem (1), (2) has a solution. In fact, the value $I(v_*, x_{0*}, x_{1*}) = 0$ if and only if the equality

$$\left.\begin{array}{c} v_*(t) + \lambda_1(t, x_{0*}, x_{1*}) + N_1(t)z(t_1, v_*) = \\ = Py(t, v_*, x_{0*}, x_{1*}) \end{array}\right.$$

is held, where

$$\left.\begin{array}{c} y(t, v_*, x_{0*}, x_{1*}) = z(t, v_*) + \lambda_2(t, x_{0*}, x_{1*}) + \\ + N_2(t)z(t_1, v_*), \\ t \in I. \end{array}\right.$$

Function $y(t, v_*, x_{0*}, x_{1*})$, $t \in I$ is solution of differential equation (6), at conditions (7), (8). Consequently,

$$\left.\begin{array}{c} \dot{y}(t, v_*, x_{0*}, x_{1*}) = A_1(t)y(t, v_*, x_{0*}, x_{1*}) + \\ + B_1(t)u_*(t) + \mu(t) = A_1(t)y(t, v_*, x_{0*}, x_{1*}) + \\ + B_1(t)Py(t, v_*, x_{0*}, x_{1*}) + \mu(t) \end{array}\right.,$$

where $u_*(t) = v_*(t) + \lambda_1(t, x_{0*}, x_{1*}) + N_1(t)z(t_1, v_*)$, $y(t_0) = x_{0*}$, $y(t_1) = x_{1*}$, $(x_{0*}, x_{1*}) \in S$, $u_*(t) \in U$. This implies, that $y(t, v_*, x_{0*}, x_{1*}) = x(t; t_0, x_{0*}, x_{1*})$, $t \in I$ is solution of the boundary value problem (1), (2). Sufficiency is proved. Theorem is proved.

As it follows from theorem 4, if the value $I(v_*, x_{0*}, x_{1*}) > 0$, then the boundary value problem (1), (2) has not solution. Thus, for constructing of a solution of boundary value problem (1), (2) necessary to solve optimization problem (21) – (23).

Lemma 2. *Let* $W_1(t_0, t_1) > 0$ *be a matrix, function*

$$F_0(q, t) = \left| v + T_1(t)x_0 + T_2(t)x_1 + \bar{\mu}(t) + N_1(t)z(t_1) - Py(t, v, x_0, x_1) \right|^2, \quad (26)$$

where

$$y(t, v, x_0, x_1) = z + C_1(t)x_0 + C_2(t)x_1 + f(t) + N_2(t)z(t_1),\ q = (v, x_0, x_1, z, z(t_1)) \in R^m \times R^n \times R^n \times R^n \times R^n.$$

Then the partial derivatives

$$\frac{\partial F_0(q, t)}{\partial v} = [2v + T_1(t)x_0 + T_2(t)x_1 + \bar{\mu}(t) + N_1(t)z(t_1) - Py], \quad (27)$$

$$\frac{\partial F_0(q,t)}{\partial x_0} = [2T_1^*(t) - 2C_1^*(t)P^*][v + T_1(t)x_0 + T_2(t)x_1 + \overline{\mu}(t) + N_1(t)z(t_1) - Py], \quad (28)$$

$$\frac{\partial F_0(q,t)}{\partial x_1} = [2T_2^*(t) - 2C_2^*(t)P^*][v + T_1(t)x_0 + T_2(t)x_1 + \overline{\mu}(t) + N_1(t)z(t_1) - Py], \quad (29)$$

$$\frac{\partial F_0(q,t)}{\partial z} = -2P^*(t)[v + T_1(t)x_0 + T_2(t)x_1 + \overline{\mu}(t) + N_1(t)z(t_1) - Py], \quad (30)$$

$$\frac{\partial F_0(q,t)}{\partial z(t_1)} = [2N_1^*(t) - 2N_2^*(t)P^*][v + T_1(t)x_0 + T_2(t)x_1 + \overline{\mu}(t) + N_1(t)z(t_1) - Py]. \quad (31)$$

Formulas (27) – (31) can be obtained by directly differentiating the function $F_0(q,t)$ by variable q.

Lemma 3. *Let $W_1(t_0,t_1) > 0$ be a matrix, set S be convex. Then:*

1) Functional (21) is convex, at conditions (22), (23);

2) Derivative

$$3)\ \frac{\partial F_0(q,t)}{\partial q} = \left(\frac{\partial F_0(q,t)}{\partial v}, \frac{\partial F_0(q,t)}{\partial x_0}, \frac{\partial F_0(q,t)}{\partial x_1}, \frac{\partial F_0(q,t)}{\partial z}, \frac{\partial F_0(q,t)}{\partial z(t_1)} \right)$$

4) satisfies to the Lipschitz condition $\left\| \frac{\partial F_0(q+\Delta q,t)}{\partial q} - \frac{\partial F_0(q,t)}{\partial q} \right\| \le L|\Delta q|, \quad \forall q,$ $q + \Delta q \in R^{m+4n}$, *where* $L = const > 0$.

Proof. It is easy to make sure that

$$F_0(q,t) = q^*E^*(t)E(t)q + 2q^*E^*(t)[\overline{\mu}(t) - Pf(t)] + [\overline{\mu}(t) - Pf(t)]^*[\overline{\mu}(t) - Pf(t)], \ t \in I,$$

where E is a matrix of $m \times 4n$ order. Then $\frac{\partial^2 F_0(q,t)}{\partial q^2} = 2E^*(t)E(t) \ge 0$ for any t, $t \in I$. Consequently, function $F_0(q,t)$ is convex with respect to q, i.e.

$$F_0(\alpha q^1 + (1-\alpha)q^2, t) \le \alpha F_0(q^1,t) + (1-\alpha)F_0(q^2,t),$$
$$\forall q^1,\ q^2 \in R^{m+4n},\ \forall \alpha,\ \alpha \in [0,1]. \quad (32)$$

For any $v_1(\cdot) \in L_2(I,R^m)$, $v_2(\cdot) \in L_2(I,R^m)$, and at all $\alpha > 0$, $\alpha \in [0,1]$ the solution of differential equation (23) under $v_\alpha(t) = \alpha v_1(t) + (1-\alpha)v_2(t)$, $t \in I$ possesses by the property

$$z(t,v_\alpha) = \alpha z(t,v_1) + (1-\alpha)z(t,v_2),\ t \in I. \quad (33)$$

In fact,

$$z(t,v_\alpha) = \int_{t_0}^{t} \Phi(t,\tau)B_1(\tau)v_\alpha(\tau)d\tau = \int_{t_0}^{t} \Phi(t,\tau)B_1(\tau)\left[\alpha v_1(\tau) + (1-\alpha)v_2(\tau)\right]d\tau =$$

$$= \alpha \int_{t_0}^{t} \Phi(t,\tau)B_1(\tau)v_1(\tau)d\tau + (1-\alpha)\int_{t_0}^{t} \Phi(t,\tau)B_1(\tau)v_2(\tau)d\tau = \alpha z(t,v_1) + (1-\alpha)z(t,v_2),\ t \in I.$$

Let $\xi_1 = (v_1(t), x_0^1, x_1^1) \in X$, $\xi_2 = (v_2(t), x_0^2, x_1^2) \in X$. Then the point

$$\xi_\alpha = \alpha\xi_1 + (1-\alpha)\xi_2 = (\alpha v_1 + (1-\alpha)v_2, \alpha x_0^1 + (1-\alpha)x_0^2, \alpha x_1^1 + (1-\alpha)x_1^2) \in X$$

The functional value

$$I(\xi_\alpha)=\int_{t_0}^{t_1}F_0\big(\alpha v_1+(1-\alpha)v_2,\alpha x_0^1+(1-\alpha)x_0^2,\alpha x_1^1+(1-\alpha)x_1^2,z\big(t,\alpha v_1+(1-\alpha)v_2\big),$$

$$z(t_1,\alpha v_1+(1-\alpha)v_2),t)dt=\int_{t_0}^{t_1}F_0\big(\alpha v_1+(1-\alpha)v_2,\alpha x_0^1+(1-\alpha)x_0^2,\alpha x_1^1+(1-\alpha)x_2^2,$$

$$\alpha z(t,v_1)+(1-\alpha)z(t,v_2),\alpha z(t_1,v_1)+(1-\alpha)z(t_1,v_2),t\big)dt\le\alpha\int_{t_0}^{t_1}F_0(\alpha q^1(t)+(1-\alpha)q^2(t))dt\le$$

$$\le\alpha\int_{t_0}^{t_1}F_0(q^1(t),t)dt+(1-\alpha)\int_{t_0}^{t_1}F_0(q^2(t),t)dt=\alpha I(\xi_1)+(1-\alpha)I(\xi_2),\ \forall\xi_1,\ \xi_2\in X.$$

In virtue by expressions (32), (33), where

$$q^1(t)=(v_1(t),x_0^1,x_1^1,z(t,v_1),z(t_1,v_1)),$$
$$q^2(t)=(v_2(t),x_0^2,x_1^2,\ z(t,v_2),z(t_1,v_2)).$$

This implies the first proposition of the lemma. Since derivative

$$\frac{\partial F_0(q,t)}{\partial q}=2E^*(t)E(t)q+2E^*(t)[\overline{\mu}(t)-Pf(t)],$$

that

$$\frac{\partial F_0(q+\Delta q,t)}{\partial q}-\frac{\partial F_0(q,t)}{\partial q}=2E^*(t)E(t)\Delta q,$$

where $\Delta q=(\Delta v,\Delta x_0,\Delta x_1,\Delta z,\Delta z(t_1))$, $E^*(t)E(t)$ is the matrix of $(m+4n)\times(m+4n)$ order with piecewise continuous elements. Then

$$\left\|\frac{\partial F_0(q+\Delta q,t)}{\partial q}-\frac{\partial F_0(q,t)}{\partial q}\right\|\le L|\Delta q|,$$

where $L=\sup\limits_{t_0\le t\le t_1}\|E^*(t)E(t)\|>0$. Lemma is proved.

Conclusion

Scientific novelty of the results is that the origin problems are reduced to the corresponding Fredholm integral equations of the first kind. Necessary and sufficient conditions for existence of a solution of the integral equations are proved by theorem. It is shown, that the boundary problem of a linear system of ordinary differential equations can be reduced to the corresponding initial optimal control problems. From the solutions of initial value problems of optimal control can be obtained the following solutions: boundary value problems with constraints, boundary problems with a parameter, construction of periodic solutions of autonomous systems. The basis of the proposed methods for solving boundary value problems with different constraints is a possibility of reducing these problems to a class of linear Fredholm integral equation of the first kind. Fredholm integral equation of the first kind belongs to the insufficiently explored problems in mathematics. Therefore, fundamental research on integral equations and solution on their basis of boundary value problems of linear ordinary differential equations is a new promising direction in mathematics.

References

1. S.A. Aisagaliev. Controllability of a differential equation system. // Differential Equations. – 1991. – Vol 27. – No. 9. – P. 1037-1045.

2. S.A. Aisagaliev., A.P. Belogurov. Controllability and speed of the process described by a parabolic equation with bounded control // Siberian Mathematical Journal. – 2012. – Vol. 53. – No. 1. – P. 13-28.

3. S.A. Aisagaliev. Controllability theory of the dynamic systems. Almaty. Kazakh university. 2014. – P. 158.

4. S.A. Aisagaliev. Controllability and Optimal Control in Nonlinear Systems // Journal of Computer and Systems. – 1994. – No. 32. – P. 73-80.

5. S.A. Aisagaliev., A.A. Kabidoldanova. Optimal control by dynamic systems // Palmarium Academic Publishing. – 2012. – Verlag. Germany. – P. 288.

6. S.A. Aisagaliev., A.A. Kabidoldanova. On the Optimal Control of Linear Systems with Linear Performance Criterion and Constraints // Differential Equations. – 2012. – Vol. 48. – No. 6. – P. 832-844.

7. S.A. Aisagaliev., T.S. Aisagaliev. Methods for solving the boundary value problems. Almaty. Kazakh university. 2002. – P. 348.

8. S.A. Aisagaliev., M.N. Kalimoldaev. Constructive method for solving a boundary value problem for ordinary differential equations // Differential Equations. – 2015. – Vol. 51. – Issue: 2. – P. 149-162.

9. S.A. Aisagaliev., Zh.Kh. Zhunussova. To the boundary value problem of ordinary differential equations // Electronic Journal of Qualitative Theory of Differential Equations. – 2015. – No. 57. – P. 1-17.

10. V.I. Smirnov. // Course of higher mathematics. M. Science. – 1974. – Vol. 4. – P. 336.

11. A.N. Kolmogorov., S.V. Fomin. Elements of the function theory and functional analysis // Science. – 1989. – P. 624.

12. M.L. Krasnov. Integral equations. Ì: Science. – 1975. – P.304.

13. A.N. Tikhonov., V.Ya. Arsenin. Methods for solving of the ill-posed problems. Ì: Science. – 1986. – P. 288.

14. M.M. Lavrentev., About some ill-posed problems of mathematical physics // RAS. – 1962. – P. 305.

15. V.K. Ivanov. On Fredholm integral equations of the first kind // Differential equations. – 1967. – Vol. 3. – No. 3. – P. 21-32.

16. V.M. Fridman. Method of successive approximations for Fredholm integral equations of the first kind // UMN XI. – 1956. – Vol. 1. – P. 56-85.

17. F.M. Mors., G. Feshbah., Methods of mathematical physics. – 1958. – Vol. 2. – P. 536.

18. S.A. Aisagaliev. General solution of a class integral equations // Mathematical journal. Institute of Mathematics MES RK. – 2005. – Vol. 5. – No. 4. – P. 7-13.

19. S.A. Aisagaliev. Constructive theory of the optimal control boundary value problems. Almaty: Kazakh university. 2007. – P. 328.

20. S.A. Aisagaliev., A.P. Belogurov. I.V. Sevrugin. To solution of Fredholm integral equations of the first kind for function with several variables // Bulletin KazNU. – 2011. – No. 1. – P. 3-16.

21. S.A. Aisagaliev. Lectures on optimal control. – Almaty: Kazakh University. 2007. – P. 278.

22. S.A. Aisagaliev., I.V. Sevrugin. Controllability and high-speed performance of processes described by ordinary differential equations // Bulletin KazNU. – 2014. – No. 2. – P. 20-37.

UDC 517.9: 004.9; 519.711.3; 504.75.05

[1]Zhakebayev D., [1]Abdibekova A., [1]Karzhaubayev K., [2]Zhubat K.

[1]Faculty of Mechanics and Mathematics, al-Farabi Kazakh National University, Almaty, Kazakhstan
[2]RSE SRC «Garish-Ecology»
*e-mail: dauren.zhakebaev@kaznu.kz

Numerical simulation of clouds formation based on the power of explosion estimated by the sizes of the funnel

Abstract. This paper considers numerical modeling of cloud formation under the action of buoyancy force, taking into account the turbulent mixing and the adiabatic expansion. Based on the solution of the three-dimensional filtered non-stationary Navier-Stokes equation, the continuity equation, the concentration equation, the enthalpy equation, and the equation of state for compressible media numerical modeling of cloud formation is carried out. The modified solver is based on the library Open Foam of solution of mathematical physics problems. To close the basic equations the viscosity model of turbulence is used. Numerical modeling of the formation of clouds formed at ground explosion of the launch vehicle "Proton-M" 2nd July 2013, shows the dependence of the fireball height from the thermodynamic parameters in the atmosphere. Comparison of the cloud rise height as a function of the explosion power with the analytic formula of Satton confirmed the applicability of the mathematical model used to the cloud formation problem in a surface explosion of a launch vehicle. The explosion power is calculated from the funnel size.

Key words: explosion, Proton-M, cloud formation, turbulence, Navier-Stokes equation, finite-volume method, large eddy simulation, fireball.

In this paper the numerical modeling of cloud formation under the action of buoyancy force is considered. The air temperature at the initial moment of the vortex ring of the cloud is very large, and over time, it falls due to adiabatic expansion, since the pressure decreases with altitude and due to turbulent mixing of heated and cold air. Under the force of buoyancy fireball heated air will rise in the atmosphere until the temperature, density due to convective and diffusive mixing of external and internal gas components of the heated and cold air is equal.

The temperature cooling due to thermal radiation can be neglected, since the length of the path of radiation is much larger than the dimensions of cloud .

Numerical modeling of the cloud formation is based on the solution of the three-dimensional filtered non-stationary Navier-Stokes equation, the continuity equation, the concentration equation, the enthalpy equation, and the equation of state for compressible media. To close the basic equations a viscous model of turbulence is used. The main problem in this task is correct the description of the turbulent transport processes. In this paper, an attempt to solve this problem by using large eddy simulation is made.

Formulation of the problem

There is a fiery half sphere at the initial moment of time at the earth surface, denoted by field G, radius R, initial temperature of ball T_1, and initial three-dimensional density of dry air's gas phases ρ_d, and humid air ρ_w, ambient temperature T_0 (picture 1).

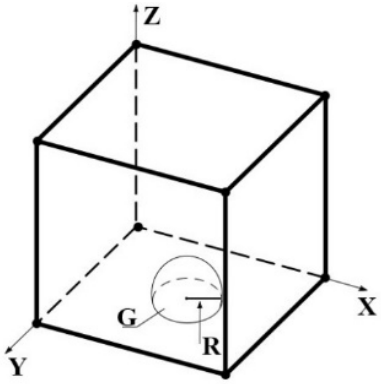

Figure 1 – Schematic illustration of the problem statement

To solve the problem the following filtered equations are used:

The equation of continuity:

$$\frac{\partial \overline{\rho}_m}{\partial t} + \nabla \cdot \left(\overline{\rho}_m \overline{u}_m \right) = 0, \qquad (1)$$

where u_m is velocity of the gas phase mixture, $\rho_m = \rho_w + \rho_d$ is air density, $\upsilon_m = \frac{\mu_m}{\rho_m}$ is dynamic viscosity, $\mu_m = \mu_* \left(\frac{T}{T_*} \right)^w$, where μ_* is the value of dynamic viscosity at temperature T_*, $\rho_d = \sum_{\alpha=1}^{N_\alpha} S_\alpha \rho_\alpha$; $\sum_{\alpha=1}^{N_\alpha} S_\alpha = 1$ is three-dimensional density of dry airs gas phase, $\rho_w = \sum_{\beta=1}^{N_\beta} S_\beta \rho_\beta$; $\sum_{\beta=1}^{N_\beta} S_\beta = 1$ three-dimensional density of the water vapors gas phase, $\rho_\alpha = \rho_{*\alpha}\left(1 - \gamma\left(T - T_*\right)\right)$, $\alpha = 1,..,N_\alpha$; $\rho_\beta = \rho_{*\beta}\left(1 - \gamma\left(T - T_*\right)\right)$, $\beta = 1,..,N_\beta$, also $\rho_{*\alpha}, \rho_{*\beta}$ are density of dry air's gas components and moist air, respectively, at $T_* = 20^0 C$.

The concentration equation:

$$\begin{aligned} &\frac{\partial \left(\rho_m S_\alpha \right)}{\partial t} + \nabla \cdot \left(\rho_m u_m S_\alpha \right) = -\nabla \cdot G_\alpha, \\ &\frac{\partial \left(\rho_m S_\beta \right)}{\partial t} + \nabla \left(\rho_m u_m S_\beta \right) = -\nabla \cdot G_\beta, \end{aligned} \qquad (2)$$

where $G_\alpha = \overline{\rho}_m \left(\overline{S_\alpha u_m} - \overline{S}_\alpha \overline{u}_m \right) = -\frac{\mu_t}{\mathrm{Pr}_t} \nabla \overline{S}_\alpha$, $\alpha = 1,..,N_\alpha$, $G_\beta = \overline{\rho}_m \left(\overline{S_\beta u_m} - \overline{S}_\beta \overline{u}_m \right) = -\frac{\mu_t}{\mathrm{Pr}_t} \nabla \overline{S}_\beta$, $\beta = 1,..,N_\beta$ describe the contribution of the sub-grid turbulent scales for gas components concentration equation.

The motion equation:

$$\begin{aligned} &\frac{\partial \left(\rho_m u_m \right)}{\partial t} + \nabla \left(\rho_m u_m \otimes u_m + \rho_m \mathbf{T}_r \right) = \\ &= -\nabla p + \nabla \cdot \mathbf{T} + \rho_m g - \nabla \cdot \mathbf{B} \end{aligned} \qquad (3)$$

where $\mathbf{B} = \overline{\rho}_m \left(\overline{u_m \otimes u_m} - \overline{u}_m \otimes \overline{u}_m \right) = \frac{2}{d} K_t \mathbf{I} - 2\mu_t \mathbf{S_m}$ - subgrid tensor responsible for small-scale structures, that need to be modeled, g – acceleration occurs under the gravity action, $\mathbf{T}$ – stress tensor of gas phase, t – time, p – pressure.

The enthalpy equation:

$$\begin{aligned} &\frac{\partial \left(\rho_m h_m \right)}{\partial t} + \nabla \cdot \left(\rho_m h_m u_m \right) + \nabla \cdot \left(q - \mathbf{T} \cdot u_g \right) = \\ &= \frac{\partial p}{\partial t} - \frac{\partial \left(\rho_m K_m \right)}{\partial t} - \nabla \cdot \left(\rho_m K_m u_m \right) + \\ &+ \rho_m (g \cdot u_m) - \nabla \cdot \left(Q + Q_K \right) \end{aligned} \qquad (4)$$

where $Q = \overline{\rho}_m \left(\overline{h_m u_m} - \overline{h}_m \overline{u}_m \right) = -\frac{\mu_t}{\mathrm{Pr}_t} \nabla \overline{h}_m$, $Q_K = \overline{\rho}_m \left(\overline{K_m u_m} - \overline{K}_m \overline{u}_m \right) = -\frac{\mu_t}{\mathrm{Pr}_t} \nabla \overline{K}_m$ - describe the contribution of the sub-grid turbulent scales [1, 2], Pr_t - turbulent Prandtl number, μ_t - turbulent viscosity, h_m - enthalpy of gas mixture, heat flux in the gas phase – $q = -k_g \Delta T$, where $k_g = \sum_{i=1}^{I} \chi_i k_i$, k_i – i-th component's conductivity, T – temperature, $K_m = \frac{1}{2}[u_m]^2$ – kinetic energy per unit mass of the gas phase.

The temperature equation:

$$T = \frac{h_m}{\frac{1}{\rho_m} \sum_{i=1}^{I} \rho_i C_i + \frac{1}{\rho_m} \sum_{i=1}^{I} \rho_i R_i} \qquad (5)$$

where C_i - heat capacity of the gas phase at constant volume.

The equation of ideal gas' state is:

$$\begin{aligned} &P = \frac{R_*}{M_{rd}} \rho_d T + \frac{R_*}{M_{rw}} \rho_w T = \\ &= R_* T \left(\frac{\rho_d}{M_{rd}} + \frac{\rho_w}{M_{rw}} \right). \end{aligned} \qquad (6)$$

where $R_* = 8.3144598$, $M_{rd} = \sum_{\alpha}^{N_\alpha} S_\alpha M_{r\alpha}$, $M_{rw} = \sum_{\beta}^{N_\beta} S_\beta M_{r\beta}$.

Initial conditions:

$$u_i(x_1, x_2, x_3, t = 0) = u_0(x_1, x_2, x_3), \ (x_1, x_2, x_3) \in G,$$

$$u_i(x_1,x_2,x_3,t=0)=0,\ (x_1,x_2,x_3)\notin G,$$

$$T(x_1,x_2,x_3,t=0)=T_1,\ (x_1,x_2,x_3)\in G,$$

$$T(x_1,x_2,x_3,t=0)=T_0,\ (x_1,x_2,x_3)\notin G,$$

$$S_\alpha(x_1,x_2,x_3,t=0)=\frac{\rho_\alpha}{\rho_m},\ \alpha=1,..,N_\alpha$$

$$S_\beta(x_1,x_2,x_3,t=0)=\frac{\rho_\beta}{\rho_m},\ \beta=1,..,N_\beta,$$

Boundary conditions:

$$\frac{\partial u_i}{\partial n}=0,\ \frac{\partial S_\alpha}{\partial n}=0,\ \frac{\partial S_\beta}{\partial n}=0,\frac{\partial T}{\partial n}=0,\ i=1,2,3,$$
$$\alpha=1,..,N_\alpha,\ \beta=1,..,N_\beta.$$

The algorithm for determining the initial value of fireball's temperature

The equation of total energy consists specific internal energy and kinetic energy. Suppose that in this problem the kinetic energy is zero.

$$E=U \tag{7}$$

where $E=0,25\cdot q\cdot t_{ex}$ - explosion energy; t_{ex} - explosion time; q - explosion power.

One-third of the energy released during the explosion is emitted in radiation form [3]. As a result, the energy enclosed in the fireball at the rise beginning is approximately one quarter of total explosion energy.

Specific internal energy in the adiabatic process is expressed by:

$$U=C_V(T_1-T_0) \tag{8}$$

where C_V - is heat capacity of gas with a constant volume, T_1 is ambient temperature for different values of fireball's initial temperature T_0.

Substituting equation (8) into equation (7), the initial value of the fireball's temperature is obtained:

$$T_0=\frac{E}{C_V}+T_1.$$

Numerical method

Three dimensional numerical simulation of equation (1) - (6) is performed with indicated initial and boundary conditions to obtain non-stationary fields of unknown variables.

The numerical algorithm based on the finite volume method on unstructured grid using the OpenFOAM class library for C++ with an open GPL license is implemented. Using C++ templates, the OpenFOAM library allows to quickly creating effective solvers and utilities for pre and post processing of modeling results due to the high level of abstraction. Classes and functions in the OpenFOAM library have implicit means for parallelizing computational procedures, due to the numerical calculation on multiprocessor computing systems does not require specific adaptations in the program code. In the finite volume method [4], partial differential equations are integrated over the volume of arbitrary cell, after the Gauss-Ostrogradsky theorem is used to translate volume integrals into surface integrals. It is necessary to interpolate unknown values on each face of finite volume, when calculating flows across finite volume boundaries. Such characteristics as accuracy and stability depend on the interpolation method's choice. Integration over time using the Crank-Nicholson scheme is carried out, the Courant number was maintained at 0.5.

Both for convective and diffusion terms implicit schemes to ensure the stability of numerical calculations were used. To bind the velocity and pressure fields the PISO procedure was used, as well as to implement the law of conservation of mass [5]. In the equations of motion and mass conservation, the explicit representations of pressure and gravity fields are used. Spatial discretization has second-order accuracy. The PISO algorithm consists of one-step of predictor and several steps of correctors. Using the pressure field from the previous time layer in the predictor step an intermediate velocity field is found. Velocity and pressure fields are corrected to increase the accuracy and reduce the mass defect in the conservation equation at each step of the corrector. The system of linear algebraic equations obtained as a result of the transport equation discretization is solved by the conjugate gradient method with the precedent of Khaletsky for the pressure equation and by the method of bi-conjugate gradients with a preconditioner of incomplete LU factorization.

Simulation results

There are results of numerical simulation of cloud formation and dynamics, formed during a surface explosion of a launch vehicle. Numerical simulation of the gas-dust cloud formation stage in the first minutes of the accident in a cubic area with the physical size of the cube edge 1280 m and the calculated grid 128x128x128 was carried out. Ground explosion is accompanied by the funnel formation at Figure 2. Funnels dimensions depend mainly on the explosion power and soil-soil type. The explosion power and depth of the funnel are related by the [6, 7]:

$$q = K_B W^3 (0,4 + 0,6n^3) \quad (9)$$

where q – explosion power; $K_в = 1{,}35$ - design specific consumption of explosives, kg / m3; W=5 – depth of the funnel, m; n=2 – explosion index.

Formula (9) allows to calculate the explosion power at a known depth of the funnel, it turned out q=0,878 t.

a) b)

Figure 2 – a) Explosion at the emergency fall place (30 seconds); b) formation of the cloud (1 minute after the explosion)

At the first seconds of the accident cloud takes on a mushroom shape, where a vortex ring on the upper part is observed, as can be seen from figure 3. At the initial time, the vortex ring's temperature is large and equal to 1800 K, for 5.5 seconds the temperature drops substantially to 400 K due to adiabatic expansion and turbulent mixing of the cloud's heated air and the environment's cold air. The drop in the cloud's temperature after 5.5 seconds occurs at a lower rate, because at these times the temperature changes due to turbulent mixing.

The fireball of heated air rises to the atmosphere until the temperature, the density due to convective and diffusive mixing of external and internal gas components of the heated and cold air are equal, under the influence of buoyancy force. Effect of thermal radiation is not taken into account while performing numerical simulation. Figure 3 shows the distribution dynamics of the mixture concentration concentration in the cloud. Figure 4 shows the change graphs in the height of the cloud rise, maximum temperature in the cloud, volume of the cloud as a time function.

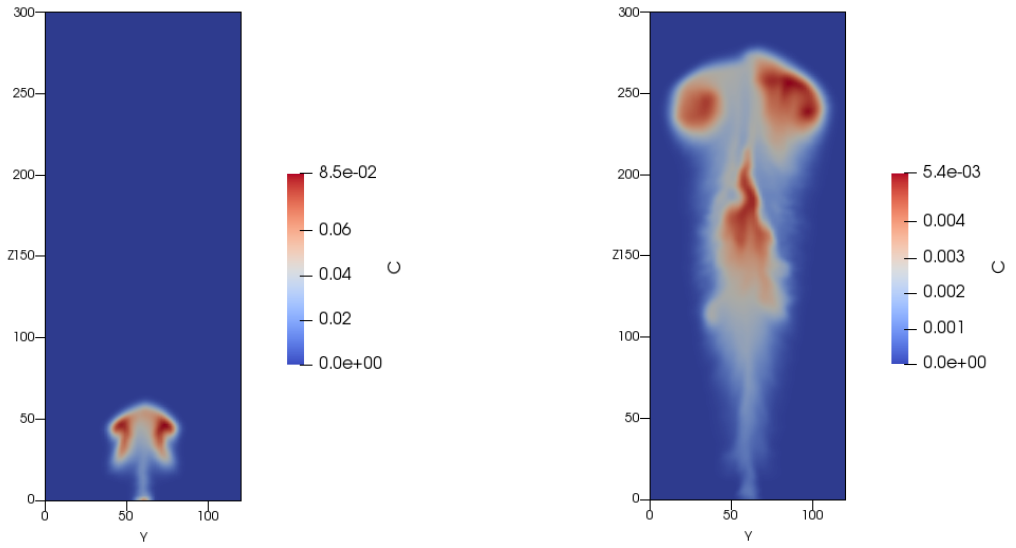

(a) (b)

Figure 3 – Distribution dynamics of the mixture concentration field at the initial value of explosion energy $E = 3.67 \cdot 10^9$ J in cross section x = 60 m: а) t = 5 sec; б) t = 35 sec.

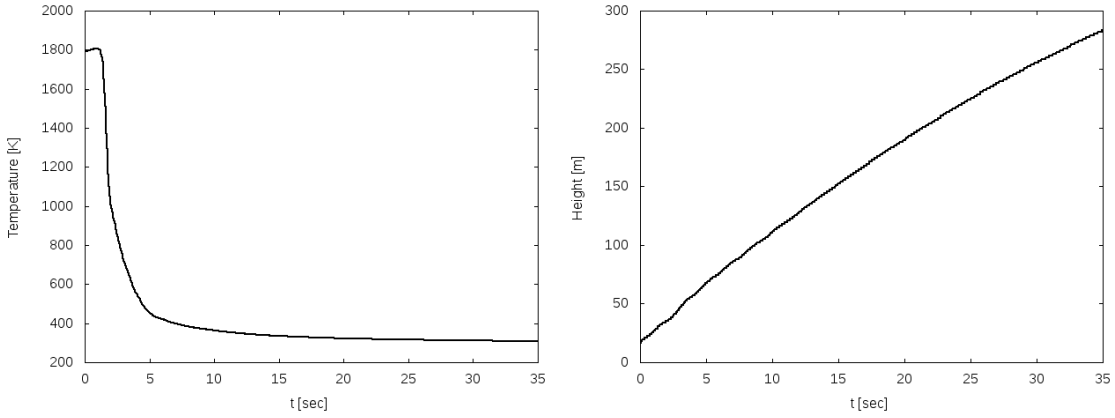

a) b)

Figure 4 – Change of a) temperature; б) the formed cloud height with the explosion power q=0.878 т.

Conclusion

The results of numerical simulation of cloud formation are obtained. The following geometric characteristics of the cloud raised as a result of the ascent are determined: the height of the uplift of the cloud, the volume of the cloud, the shape of the vortex ring in the cloud. Comparison of the cloud rise height as a function of the explosion power with the analytic formula of Satton confirmed the applicability of the mathematical model used to the cloud formation problem in a surface explosion of a launch vehicle. The explosion power is calculated from the funnel size.

In conclusion, we note that the results of this study allow us to estimate the geometric characteristics of raised cloud, the concentration of gas components mixture in the cloud at different instants of time. Such an opportunity is invaluable in absence of experimental data on the cloud formed as a result of an accident. The obtained results allow conducting a primary assessment of the accident impact on the environment.

References

1. F. Nicoud., F. Ducros: Subgrid-scale stress modelling based on the square of the velocity gradient tensor // Flow Turbul. Combust. – 1999. – Vol. 62. – P. 183–200.

2. F. Piscaglia., A. Montorfano., A. Onorati: Towards the LES simulation of IC engines with parallel topologically changing meshes // SAE Int. J. Engines. – 2013. – Vol. 6. – P. 926–940.

3. A.T. Onufriev. The theory of motion of a vortex ring under the action of gravity. Rise of the cloud of the atomic explosion // PMTF. – 1967. – № 2. – P. 3–15.

4. Ferziger. Perić. Computational Methods for Fluid Dynamics. – 3. rev. ed. – Berlin; – 2002.

5. R.I. Issa., A.D. Gosman., A.P. Watkins. The Computation of Compressible and Incompressible Recirculating Flow by a Non–Iterative Implicit Scheme // Journal of Computational Physics. – 1986. – Vol. 62. – P. 66–82.

6. Ed. F. Avdeeva. Technical rules for blasting operations on the day surface // – M: Nedra. – 1972. – P. 239.

7. L.P. Orlenko. // Physics of the explosion – Moscow: – FIZMATLIT. – 2002. – Ed. 3rd. revised. – Vol. 1. – P. 832.

UDC 539.2: 669

[1*]Komarov F., [1]Vlasukova L., [1]Makhavikou M.,
[2]Wendler E., [3]Togambayeva A.

[1]Institute of Applied Physics Problems BSU, 7 Kurchatova str., 220045 Minsk, Belarus,
[2]Friedrich-Schiller-Universität, Max-Wien-Platz 1, D-07743 Jena, Germany
[3]Al-Farabi Kazakh National University, NNLOT, al-Farabi 71, 050040 Almaty
e-mail: komarov@bsu.by

Formation of ZnSe nanoclusters in the layers of silicon dioxide by high-fluence ion implantation and annealing

Abstract. In this work we used the method of "hot" implantation of zinc and selenium ions into SiO2 / Si structures in combination with subsequent heat treatment in order to form nanosized phases. Implantation modes for ionic synthesis chosen in such a way that the concentration of the embedded impurity is maximum approximately at the middle of the thickness of the dielectric layer. For the subsequent clustering of the impurity, it is necessary to create a high concentration of the implanted impurity at the maximum of the depth profile. The computer stimulation to select Implantation modes was carried out using the SRIM-2013 program. Also we calculated the thickness of the silicon dioxide layer sprayed during high-dose implantation of zinc ions was. In this way, we have studied the formation of ZnSe precipitates in silicon dioxide by means of Zn (150 keV, 4×1016 cm−2) and Se (170 keV, 4×1016 cm−2) implantation at 550 °C and subsequent annealing at 1000 °C for 3 min. From analysis of XTEM images it has been showen that the use of "hot" implantation leads to the formation of small nanoclusters with sizes from 2 to 15 nm. Subsequent annealing results in the redistribution of nanoclusters within the implanted layer and the formation of large crystallites (up to 80 nm). To analyze the distribution of the introduced impurity throughout the sample depth the Rutherford backscattering (RBS) method was used. The band at 251-256 cm-1 associated with LO phonons of crystal ZnSe was registered in Raman spectra.
Key words: Ion Implantation, nanoclusters, precipitates, silicon dioxide, zinc ions.

Introduction

Investigations aimed at the development of new light-emitting elements and devices based on silicon technology draw increasingly greater attention. Silicon is an indirect-gap semiconductor, and, as a result, has a low quantum efficiency of interband radiative recombination. Therefore, at the present time, various methods and approaches are used to create silicon-based light-emitting structures: creation of Si / SiO_2 superlattices [1], formation of silicon/germanium structures [2], silicon or germanium nanoprecipitates in SiO_2 [3,4], formation of nanocrystals of A^3B^5 compounds in silicon [5], and A^2B^6 compounds in SiO_2 [6]. In order to create new optoelectronic devices, A^2B^6 compounds based on chalcogenides, such as ZnS, CdSe, CdTe, and ZnSe, attracted great interest of scientific groups. This type of compounds has a direct-gap semiconductor structure and is now widely used for creation of lasers [7], solar cells [8], monochrome and white LEDs [9]. A perspective direction is combination of optical characteristics of these compounds with instrument silicon structures.

Zinc selenide (ZnSe) is of interest as a promising luminescent material for creation of various optoelectronic elements used in the visible and infrared spectral ranges, as well as in optical and laser CO_2 optics [10]. In works [11-12] it was reported about the creation of devices based on wide-gap semiconductors of ZnS and zinc selenide (ZnSe). Zinc selenide can be used for inorganic passivation [11] of various nanoclusters (quantum dots) to form a core-shell structure. Alloying of ZnS with various impurities gives electroluminophores with green, red and blue emission bands [12], the composition of which enables us to create an electroluminescent indicator with white light.

In this work ion-beam synthesis was used to form nanoscale inclusions of zinc selenide in silicon dioxide. It was assumed that the use of high-dose implantation of zinc and selenium ions in combination with subsequent heat treatment would enable us to synthesize extended layers of ZnSe nanoclusters in the SiO_2 matrix.

 Printed in Kazakhstan

Experimental conditions

In this work we used the method of "hot" implantation of zinc and selenium ions into SiO_2 / Si structures in combination with subsequent heat treatment in order to form nanosized phases.

The original 2 × 2 cm^{-2} samples were cut out from thermally oxidized SiO_2 (600 nm) / Si silicon wafers and implanted with ions under computer-simulated (SRIM-2013) modes in order to create a comparable concentration of zinc and selenium atoms at a given depth in the SiO_2 layer. Two groups of samples were made. For the first group, double implantation of ions in the SiO_2 (600 nm) / Si structure was made in the Zn ↓ (150 keV, 4 × 10^{16} cm^{-2}) + Se ↓ (170 keV, 4 × 10^{16} cm^{-2}) sequence. In the second part of the samples, the order of implantation was changed: Se ↓ + Zn ↓. For all samples, implantation was carried out at a temperature of 550 ° C - "hot" conditions. Post-implantation annealing was made in an argon atmosphere at 1000 ° C for 3 minutes.

To analyze the distribution of the introduced impurity throughout the sample depth the Rutherford backscattering (RBS) method was used.

The RBS spectra were recorded on the electrostatic accelerator complex AN-2500, created in the laboratory of elionics of the NIIPPP at A.N. Sevchenko Belarusian State University. From the experimentally obtained RBS spectra, profiles of impurity distribution in implanted SiO_2/Si structures were calculated. The profiles were calculated by modeling the RBS spectra using the HEAD software package until they completely coincided with the experimental spectra. When calculating the impurity profiles, the silicon oxide film was divided into several layers in order to more accurately determine the concentration of atoms over the thickness of the silicon dioxide layer.

Structural-phase transformations were studied by transmission electron microscopy (TEM) using a HitachiH-800 electron microscope with an accelerating voltage of 200 keV in the cross-section and Raman scattering geometry. The samples were prepared in two stages: mechanical polishing using the GATAN preparation system and subsequent thinning by ion etching.

Results of investigation

Implantation modes for ionic synthesis should be chosen in such a way that the concentration of the embedded impurity is maximum approximately at the middle of the thickness of the dielectric layer. For the subsequent clustering of the impurity, it is necessary to create a high concentration of the implanted impurity at the maximum of the depth profile.

Computer simulation of implantation of zinc ions into the SiO_2/Si structure in silicon dioxide was carried out using the SRIM-2013 program.

In the course of the work, it was planned to implant zinc and selenium ions into thin (less than 90 nm thick) and thick (300 - 900 nm) layers of silicon dioxide. Therefore, profiles were simulated for different energies of the implanted ions and doses in the range (5-10) × 10^{16} cm^{-2}.

The distribution of the implanted impurity in the SiO_2 and Si matrices was simulated for the energies of zinc ions from 80 to 200 keV. Figure 1 shows the calculated depth profiles of zinc impurity distribution in the SiO_2 matrix (SiO_2/Si structure with a 600 nm layer of silicon dioxide).

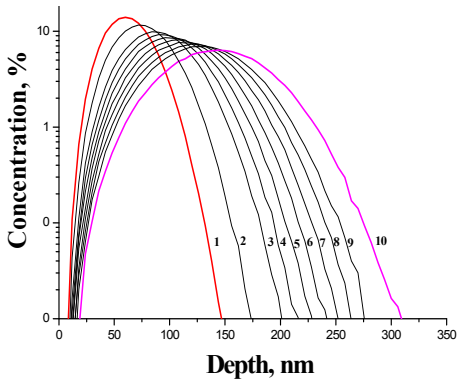

Figure 1 – Calculated (SRIM-2013) depth profiles of distribution of the impurity in silicon dioxide implanted with zinc ions with an energy of 80 (1), 100 (2), 120 (3), 130 (4), 140 (5), 150 (6), 160 (7), 170 (8), 180 (9), and 200 keV (10) at a dose of 4×10^{16} cm^{-2}

It can be seen from the figure that at the same dose of implantation, the zinc concentration at the maximum of the depth profile increases as the ion energy decreases. Thus, at an energy of 80 keV and a dose of 4 × 10^{16} cm^{-2} of zinc ions, respectively, the maximum concentration of zinc atoms in silicon dioxide at a depth of about 60 nm is about 15 at.%. For the same dose at an ion energy of 200 keV, the maximum concentration of zinc atoms in silicon dioxide at a depth of ~ 140 nm is about 7 at.%.

Thus, in accordance with the simulation data, the concentration of the implanted zinc impurity in silicon dioxide was changed from 7 to 30 at.% by changing the energy and ion doses in the ranges (80-200 keV) and (4-10) x 10^{16} cm^{-2}.

The thickness of the silicon dioxide layer sprayed during high-dose implantation of zinc ions was also

calculated. The calculation was carried out using the formula:

$$D_{distr} = \frac{Y}{N} \cdot D \quad (1)$$

where Y is the sputtering coefficient, N is the matrix density, and D is the implantation dose of the impurity ions.

The density of silicon dioxide was assumed to be 2.3 g / cm^3, which corresponds to 6.915 × 10 ^{23} at / cm^3.

Figure 2 shows the TEM micrograph (Figure 2A) of the cross section and the Raman spectrum (Figure 2B) of the SiO_2 layer immediately after implantation of the impurity in the sequence Zn ↓ + Se ↓. Under the near-surface layer of oxide free from precipitates (thickness 20-40 nm), there is an extended layer (40-190 nm from the surface) containing a large number of small clusters with sizes from 2 to 15 nm. At the center of this layer (region Rp ~ 100 nm) clusters are larger, their sizes are 8-15 nm. A similar picture was observed in our work [11], where larger clusters were formed in the region of a larger impurity concentration during implantation of zinc ions into the layers of silicon dioxide.

The Raman spectrum has two peaks. The intense narrow band at ~300 cm^{-1} corresponds to the well-known second-order Raman band (2TA) from the silicon substrate. The second peak with a maximum at 251-256 cm^{-1} corresponds to scattering by a longitudinal optical phonon (LO-mode) in crystalline ZnSe [12-14].

Thus, after implantation of zinc and selenium ions at a substrate temperature of 550 □, the ZnSe phase is formed, which in the matrix of silicon dioxide forms tiny nanoprecipitates recorded on TEM images.

A similar situation is observed in the samples with a different sequence (Se ↓ + Zn ↓) of implantation of an impurity in SiO_2 under the same "hot" implantation conditions (Figure 3). In this case, the thickness of the layer containing small (from 2 nm and larger) nanoclusters is noticeably smaller (the layer lies at a depth of about 20-140 nm from the surface), and the cluster sizes near R_p are larger (10-20 nm). It can be assumed that the selenium atoms implanted first prevent zinc diffusion into the depth of the sample during subsequent implantation due to formation of a ZnSe compound in which Zn atoms are less mobile. Localization of the impurity in a narrower layer also leads to an increase in the size of precipitates of the crystalline ZnSe phase, the presence of which is indicated by a peak near 251-256 cm^{-1} in the Raman spectrum (Figure 2B). It can be noted that in this case the intensity of this peak is lower than for the sequence (Zn ↓ + Se ↓) of implantations. The lower intensity of this peak can be explained both by the smaller fraction of formed ZnSe phase and by the greater number of structural defects in the precipitates (in comparison with the first sequence of introduction of impurities into the samples).

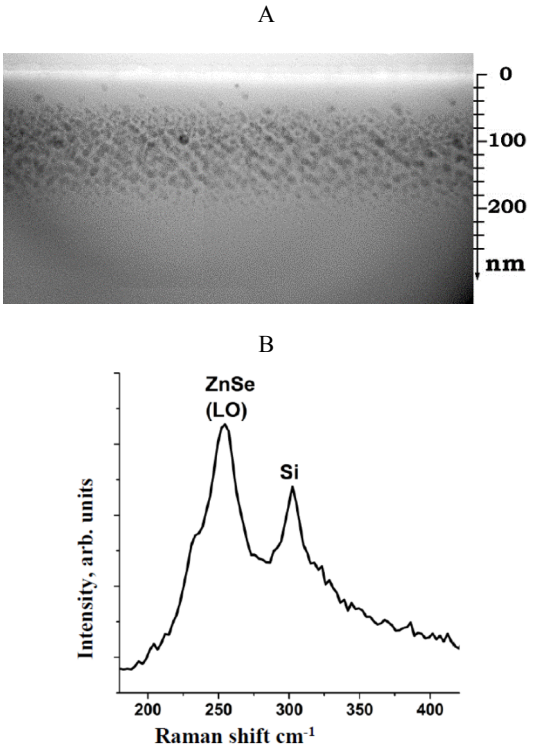

Figure 2 – TEM microphotograph of the cross section (A) and the Raman spectrum (B) after "hot" implantation of the impurity in the sequence Zn ↓ + Se ↓ into the SiO_2 layer

Figure 4 shows TEM-microphotographs of sample cross-sections after high-temperature annealing. It can be seen that there is a significant rearrangement of the structure of clusters for two samples with different sequences of impurity implantations.

The number (density) of clusters in the silicon dioxide layers sharply decreases, but their size substantially increases (up to 50-60 nm). Clusters are characterized by a regular faceted shape, and secondary structure defects (twin boundaries) are noticeable, which indicates their crystal structure. For the sample with the first type of implantation sequence (Zn ↓ + Se ↓), the depth shift of large clusters from the R_p region (~ 100 nm) to the surface (to a depth of ~ 60-70 nm) can be noted. Smaller (20-

40 nm) single clusters are recorded in other regions of the sample, which can be traced down to the SiO_2 (600 nm)/Si structure boundary. In the second sample (with the sequence of implants (Se ↓ + Zn ↓) large clusters near R_p were formed after heat treatment, in this case, single clusters with smaller dimensions in other places of the oxide layer were practically not registered, but in some spots on the surface of the sample release of impurities (Figure 2B - arrow), presumably, selenium was observed.

Raman spectra from samples after high-temperature annealing (Figure 5) are very similar to the spectra of samples immediately after implantation. Only 2 peaks are recorded: one is associated with the silicon substrate, the other – with the longitudinal mode of the optical phonon (LO-mode) in crystalline ZnSe.

The intensity of the band associated with the (LO)-mode of the optical phonon in ZnSe after heat treatment, like for samples immediately after implantation, is much lower for the sample with the second implantation sequence. This enables us to speak of a smaller amount of the ZnSe phase in this case.

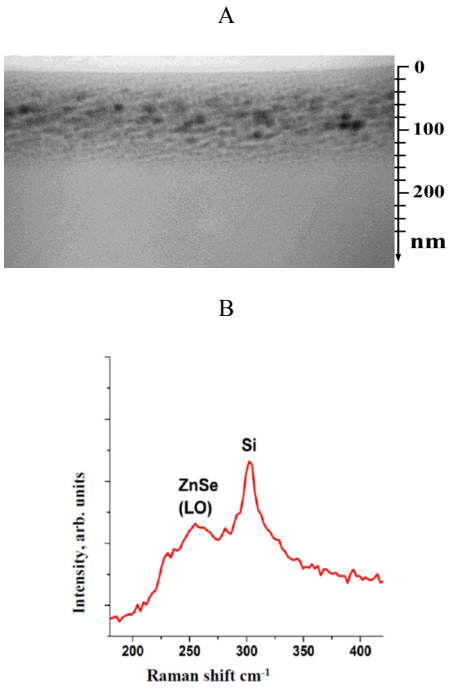

Figure 3 – TEM microphotograph of the cross section (A) and the Raman spectrum (B) after "hot" implantation of the impurity in the sequence Se ↓ + Zn ↓ into the SiO_2 layer

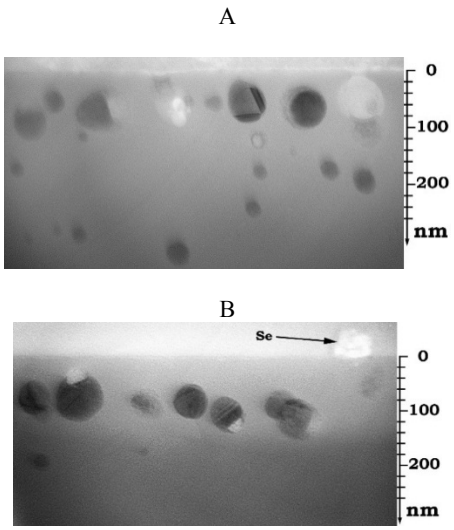

Figure 4 – TEM-microphotographs of the cross-section of SiO_2 layers after 550 ° C implantation: A - Zn + Se, B - Se + Zn; and after annealing in the BTT mode (1000 ° C, 3 min, Ar)

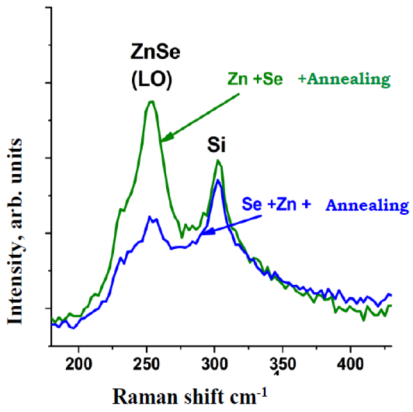

Figure 5 – Raman spectra from SiO_2 layers after 550 ° C implantation and annealing in BTT mode (1000 ° C, 3 min, Ar)

Conclusion

The structural and phase characteristics of silicon dioxide layers after high-dose implantation (at 550 ° C) of zinc and selenium ions with subsequent heat treatment have been studied. It was established that the use of "hot" implantation conditions leads to formation of small (2-15 nm) nanoclusters immediately after implantation of zinc and selenium ions. Subsequent high-temperature heat treatment leads to structural rearrangement and increase in cluster sizes (up to 80 nm).

In the Raman spectra of the samples, both immediately after implantation and after heat treatment, a band at 251-256 cm^{-1}, which corresponds to scattering by a longitudinal optical phonon (LO mode) of crystalline ZnSe, is registered.

This work was supported by the BRFFR grant for young scientists No. F17M-053.

References

1. X. Luo., S. B. Zhang., S. H. Wei. Chemical Design of Direct-Gap Light-Emitting Silicon // Phys. Rev. Lett. – 2002. – Vol. 89. – P. 076802.

2. L. Vescan., T. Stoica. Room-temperature SiGe light-emitting diodes // J. Luminescence. 1999. V. 80 P. 485-489.

3. F.L. Bregolin., M. Behar., U.S. Sias., E.C. Moreira. Photoluminescence induced from hot Ge implantation into SiO2 // Nucl. Instr. Meth. B. – 2009. – Vol. 267. – P. 1321-1323.

4. L. Rebohle. J. Von Borany. H. Fröb. W. Skorupa. Blue photo- and electroluminescence of silicon dioxide layers ion-implanted with group IV elements // J. Appl. Phys. B. 2000. V. 71. P. 131-151.

5. F.F. Komarov., L.A. Vlasukova., W. Wesch. et al. Influence of implantation and therapeutic modes for visible photoluminescency Zn (Se, S) nanoclusters in SiO2 // Nucl. Instr. Meth. B. – 2008. – Vol. 266. – P. 3557-3564.

6. I. D. Desnica-Frankovic., P. Dubcek. et. al. Influence of stoichiometry deviations on properties of ion-beam synthesized CdSe QDs // Nucl. Instr. Meth. B. 2005. V. 238. P. 302-305.

7. M.A. Haase., J. Qiu., J.M. Depuydt., H. Cheng Blue-green laser diodes // Appl. Phys. Lett. – 1991. – Vol. 59. – P. 1272.

8. H. Babucke., P. Thiele., T. Prasse., M. Rabe., F. Henneberger ZnSe-based electro-optic waveguide modulators for the blue-green spectral range // Semiconductor Science and Technology. – 1998. – Vol. 13. –P. 200-206.

9. I.K. Vereshchagin., B.A. Kovalev., L.A. Kosyachenko et. al. Elektrolyuminestsentnyye istochniki sveta // M.: Energoatomizdat. – 1990. – P. 168.

10. C.K.N. Patel. Continius-wave laser action on vibrational-rotational transitions onCO2 // Physical Review. – 1996. – Vol. 136. – P. A1187–A1193.

11. M. Makhavikou., F. F. Komarov., L. A. Vlasukova. et al. High Temperature Material Processes: An International Quarterly of High-Technology Plasma Processes. – 2014. – Vol. 18. – P. 255-261.

12. K. Shahad., D.J. Olego., C.G. Van De Walle., D.A. Cammack. Effects of strain on the optical and vibrational properties of ZnSe-ZnSxSe1-x strained-layer superlattices // J. Luminescence. 1990. V. 46. P. 109-136.

13. S. Itoh., K. Nakano. A. Ishibashi Current status and Future prospects of ZnSe-based light-emitting devices // Journal of Crystal Growth. – 2000. – Vol. 214. – P. 1029-1034.

14. K.T. Yong. Mn-doped near-infrared quantum dots as multimodal targeted probes for pancreatic cancer imaging // Nanotechnology. – 2009. – Vol. 20. – P. 1-10.

UDC 533.9

[1*]Arkhipov Yu.V., [1]Ashikbayeva A.B., [1]Askaruly A., [1]Dubovtsev D.Yu.,
[1]Syzganbayeva S.A., [2]Tkachenko I.M. [2]

[1]Department of Plasma Physics, al-Farabi Kazakh National University, Tole Bi 96, Almaty 050012, Kazakhstan,
[2]Departamento de Matemática Aplicada, Universitat Politècnica de València,
Camino de Vera s/n, 46022 Valencia, Spain
[*]e-mail: yarkhipov@yahoo.ca

Optical properties of dense coulomb plasmas

Abstract. In the present work, we provide a theoretical analysis of the reflection of low-temperature dense plasma for the normal incidence of laser radiation, and the dependence of reflectivity of s - and p - polarized waves in respect to the angle of incidence. In connection with the calculations for large parameters of density, the interpolation approach based on the theory of moment's method is used for the calculation of the dielectric function. In contrast to the classical method of moments, the characteristic frequencies can be found from the simplified formulas, and the Nevanlinna parameter function is determined as in Phys.Rev.Lett. 119, 045001 (2017). The reflectivity is calculated with using of Fresnel equations. The obtained results were compared with theoretical and experimental data of other authors. It is shown that results of the present work for the reflection coefficient are close to the experimental results, in contrast to other theoretical results, in which a model with several adjustable parameters was used. The patent of RK for the present method was submitted.
Key words: dense Coulomb plasmas, reflectivity, dielectric function, method of moments.

Introduction

Nonideal plasma is the most common state of matter in the Universe. For instance, warm dense matter is formed: in giant planets cores; in the process of the electrical explosion of conductors; in the matter impacted by femtosecond laser pulse; at moving of swift heavy ion through a nuclear material etc. For further development of nonideal plasma physics, investigations of its electronic properties appear to be crucial. In particular, optical reflectance are an important diagnostic tool: the reflectivity is expected to give information on the free-charge carrier density. The reflectance of the shock-compressed xenon is measured in the unique experiments of Mintsev and Zaporozhets [1-4]. The main purpose of this work is the theoretical explanation of the experimental data using the interpolation method of moments. Because this method allows you to find the dielectric function of plasma on the basis of exact relations and sum rules (frequency moments of the imaginary part of the dielectric function) directly through interpolation static characteristics of the system.

Let us specify the thermodynamic parameters characteristic of model plasmas we deal with. Consider model completely ionized hydrogen-like plasmas in thermal equilibrium. The number density of electrons, n_e is presumed to be of the order of 10^{21} cm^{-3}, the temperature, T , so that $\beta^{-1}=k_BT$. Under these conditions all characteristic lengths in the system are of the same order of magnitude and the dimensionless parameters, like $\Gamma=\beta e^2/a$, ($a=(3/4\pi n)^{1/3}$ being the Wigner-Seitz radius) and the density parameter, $r_s=a/a_B$, a_B - Bohr radius.

Self – consistent calculation method

The Fresnel formulas [5] are used for calculation of reflectivity for the normal incidence ($\theta = 0^0$) of the electromagnetic wave

$$R = \left|\frac{(\sqrt{\epsilon}-1)}{(\sqrt{\epsilon}+1)}\right|^2, \qquad (1)$$

and for the s- and p-polarized reflectivity

$$R_s = \left(\frac{\left|cos\theta - \sqrt{\epsilon - sin^2\theta}\right|}{\left|cos\theta + \sqrt{\epsilon - sin^2\theta}\right|}\right)^2,$$

$$R_p = \left(\frac{\left|\epsilon\, cos\theta - \sqrt{\epsilon - sin^2\theta}\right|}{\left|\epsilon\, cos\theta + \sqrt{\epsilon - sin^2\theta}\right|}\right)^2. \qquad (2)$$

The dielectric function ϵ (DF), which is included in (2) and (1) is a complex function and can be expressed as

$$\epsilon^{-1}(k,\omega) = 1 + \frac{\omega_p^2(\omega + Q(k,\omega))}{\omega(\omega^2 - \omega_2^2(k)) + Q(k,\omega)(\omega^2 - \omega_1^2(k))} \ . \quad (3)$$

In general, the characteristic frequencies $\omega_1(k)$ and $\omega_2(k)$ can be calculated on the basis of the Kubo theory of linear response [6], but here, for simplicity and as a tool of preliminary but reliable estimate, we employ for them the following interpolation expressions [7,8]:

$$\omega_1^2(k) = \omega_p^2(1 + k^2 k_D^{-2} + k^4 \varkappa^4) \quad (4)$$

in a hydrogen-like plasma with

$$n_e = Zn_i,$$

n_i-density of protons,

$$\varkappa^4 = \frac{16\pi e^2}{\hbar^2} a^4 (n_e m_e + Z^2 n_i m_i) \approx$$

$$\approx \frac{16\pi Z^2 e^2 n_i a^4 m_i}{\hbar^2} = 12 r_s \frac{m_i}{m_e}.$$

$$\omega_2^2(k) = \omega_p^2(1 + H) +$$

$$+\langle v_e^2 \rangle k^2 + (\hbar k^2/2m_e)^2 - v_{int}^2 k^2. \quad (5)$$

The parameters introduced here (4,5) can be calculated immediately: $v_{int}^2 = -\frac{4}{15}\frac{\Gamma^{\frac{3}{2}}}{\beta m_e}\left(\frac{A_1}{\sqrt{A_2+\Gamma}} + \frac{A_3}{1+\Gamma}\right)$, $A_1 = -0{,}9052, A_2 = 0{,}6322$ и $A_3 = \frac{-\sqrt{3}}{2} - \frac{A_1}{\sqrt{A_2}}$, $\hbar$ – Planck constant, e – charge of electron, ω_p – the plasma frequency, $\langle v_e^2 \rangle$ – the average square of the electron thermal velocity, k_D^{-1} – the Debye radius, and m_e – electron mass and m_i – proton mass; Finally, the contribution H is related to the electron-ion interaction in the target plasma and we evaluate it in the modified random-phase approximation [9] as: $H = (4r_S/3)(3\Gamma + 4r_S/\Gamma + 4\sqrt{6r_S})^{-1/2}$.

In the present work, we do not reconstruct the Nevanlinna parameter function (NPF) from the very data, we use the following NPF model [10], where $q = ka$:

$$Q(q,\omega) = ih_0(q)), \quad (6)$$

where the positive parameter $h_0(q)$ is a function of the frequencies $\omega_2^2(q)$ and $\omega_1^2(q)$.

Numerical results

The analytical results of the reflectivity coefficient R^{IMM} (1) at the plasma front, depending of the incident angle θ in comparison with experimental data at the R^{exp} [11] wavelengths of λ_L = 1064 nm, λ_L = 694 nm, λ_L = 532 nm and the respective thermodynamic parameters are presented in tables 1, 2 and 3 (pressure P, temperature T, mass density ρ, density of free electrons n_e, density of neutral atoms n_a, ionization degree $\alpha_{ion} = \frac{n_e}{(n_a+n_e)}$ and degeneracy parameter $\Theta = \frac{k_B T}{E_F}$, E_F – Fermi energy.)

Table 1 – λ_L = 1064 nm

P, (GPa)	T, (K)	ρ, g/cm-3	$n_e \cdot 10^{21}$ cm-3	$n_a \cdot 10^{21}$ cm-3	α_{ion}	Γ	Θ	R^{exp}	R from [12]	R^{IMM}
1.6	30050	0.51	1.8	6.1	0.75	1.1	4.8	0.096	0.272	0.14
3.1	29570	0.97	3.2	1.4	0.70	1.3	3.2	0.12	0.342	0.18
5.1	30260	1.46	4.5	2.2	0.67	1.5	2.6	0.18	0.381	0.20
7.3	29810	1.98	5.7	3.5	0.62	1.6	2.2	0.26	0.404	0.23
10.5	29250	2.70	7.1	5.4	0.57	1.8	1.9	0.36	0.429	0.25

Table 2 – λ_L= 694 nm

P , (GPa)	T, (K)	ρ, g/cm-3	$n_e \cdot 10^{21}$ cm-3	$n_a \cdot 10^{21}$ cm-3	α_{ion}	Γ	Θ	R^{exp}	R^{IMM}
0.93	32070	0.27	1.1	2.1	0.78	0.87	7.1	0.02	0.039
1.9	32900	0.53	2.1	4.8	0.72	1.0	4.8	0.05	0.11
4.1	33100	1.1	4.0	1.3	0.69	1.3	3.2	0.11	0.15
6.1	33120	1.6	5.2	2.1	0.64	1.4	2.6	0.14	0.18
9.1	32090	2.2	6.6	3.6	0.60	1.6	2.1	0.18	0.19
12.0	32020	2.8	7.8	5.0	0.56	1.7	1.9	0.26	0.21

Table 3 – λ_L = 532 nm

P , (GPa)	T, (K)	ρ, g/cm-3	$n_e \cdot 10^{21}$ cm-3	$n_a \cdot 10^{21}$ cm-3	α_{ion}	Γ	Θ	R^{exp}	R^{IMM}
4.1	33100	1.1	4.0	1.3	0.69	1.3	3.2	0.02	0.1
6.1	33120	1.6	5.2	2.1	0.64	1.4	2.6	0.045	0.15
9.1	32090	2.2	6.6	3.6	060	1.6	2.1	0.10	0.17
12.0	32020	2.8	7.8	5.0	0.56	1.7	1.9	0.16	0.18

On the pictures (1,2) one can see theoretical values the reflectivity of electromagnetic waves, 532 Nm and 694 Nm of length with different kinds of polarization (s-p) from the dense plasma`s surface and experiment data, as seen from the graphs, there is a good agreement.

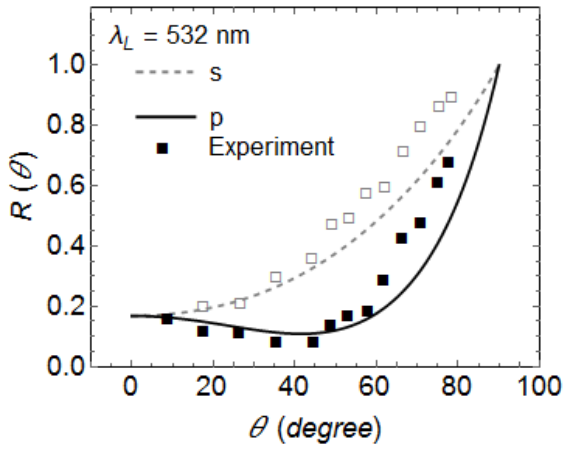

Figure 1 – Calculated reflectivity (1) in comparison to the experimental data for λ_L = 532 nm. *s*-polarisation is gray dashed line, *p*-polarisation is black line. Experimental data [13] are shown as square.

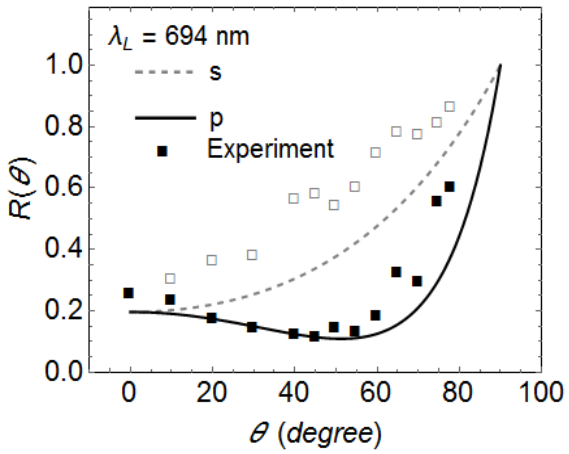

Figure 2 – Calculated reflectivity (1) in to the experimental data for λ_L = 694 nm. *s*-polarisation is gray dashed line, *p*-polarisation is black line. Experimental data [13] are shown as square.

4 Conclusions

This simplified mathematical method of moments allows describing theoretically the optical properties of dense Coulomb systems. From the results of Tab.1-3, one can see that the reflection coefficient, calculated in the present article is closest to the experimental data [11], in contrast to the approach from [12] and other theoretical results, where a model with several adjustable parameters was used.

Acknowledgements.

Work supported by the Republic of Kazakhstan Ministry of Education and Science grant No. 3119/GF4 and No. 3831/GF4.

References

[1] V.B. Mintsev., Yu.B. Zaporogets // Contrib. Plasma Phys. – 1989. – Vol. 29. – N. 4. – P. 493 – 501.

[2] Yu. B. Zaporoghets., V. B. Mintsev., V. K. Gryaznov., V. E. Fortov. // Physics of Extreme States of Matter - 2002. Chernogolovka. – 2002. – P. 188 – 189.

[3] Yu. B. Zaporoghets., V.B. Mintsev., V.K. Gryaznov., H. Reinholz., G. Röpke. // Physics of Extreme States of Matter. – 2004. Chernogolovka. – P. 140 – 141.

[4] Yu. B. Zaporoghets., V.B. Mintsev., V.K. Gryaznov., H. Reinholz., G. Röpke., V. E. Fortov. // Physics of Extreme States of Matter. – 2013. Chernogolovka. – P. 194 – 197.

[5] Yu.L. Klimontovich. Kinetic theory of nonideal gas and nonideal plasma // M: Nauka. – 1975. – P. 352

[6] Yu. V. Arkhipov et al. // Phys. Rev. E. – 2014. – Vol. 90. – P. 053102; *ibid* – 2015. – Vol. 91. – P. 019903

[7] V.M. Adamyan., I.M. Tkachenko // High Temp. – 1983. – Vol. 21. – P. 307; J. Ortner I.M. Tkachenko // Phys. Rev E. – 2001. – Vol. 63. – P. 0264031-11.

[8] G. Chabrier., A. Y. Potekhin. Equation of state of fully ionized electron-ion plasmas //Phys. Rev. E. – 1998. – Vol. 58. – P. 4941.

[9] M.J. Corbatón., I.M. Tkachenko // International Conference on Strongly Coupled Coulomb Systems. – 2008. Camerino. Italy. Book of Abstracts. – P. 90.

[10] Yu. V. Arkhipov *et al*. Direct Determination of Dynamic Properties of Coulomb and Yukawa Classical One-Component Plasmas // Phys.Rev.Lett. – 2017. – Vol. 119. – P. 045001.

[11] Yu. Zaporoghets., V. Mintsev V., Gryaznov V., Fortov., H. Reinholz., T. Raitza., G. Ropke. Reflectivity of nonideal plasmas // J. Phys. A: Math. Gen. – 2006. – Vol. 39. – No 17. – P. 4329-4335.

[12] Yu. B. Zaporozhets., Y. A. Omarbakiyeva., H. Reinholz., G. Ropke., V. B. Mintsev., V. K. Gryaznov. Optical Reflectivity of Xenon Plasma Revisited // Contribution of the 15th International Conference on the Physics of Non-Ideal Plasmas. – 2015. Kazakhstan. Almaty.

UDC 621.383

[1]Paunkov N., [2*] Popov R., [3]Manatbayev R., [3]Kalasov N.,
[3]Zulbuharova E., [3]Tulepbergenov A., [4]Nedelcheva S., [5]Georgiev A.

[1]Faculty of Electronics and Automation, Technical University of Sofia, Plovdiv Branch, Bulgaria
[2]Plovdiv university Paisii Hilendarski, Plovdiv, Bulgaria
[3]Physico-Technical Faculty, al-Farabi Kazakh National University, Almaty, Kazakhstan
[4]Faculty of Engineering and Pedagogy - Sliven, Technical University of Sofia, Bulgaria
[5]Faculty of Mechanical Engineering, Technical University of Sofia, Plovdiv Branch, Bulgaria
[*]e-mail: rum_pop@yahoo.com

Efficiency comparison of photovoltaic and photovoltaic-thermal solar panels

Abstract: The photovoltaic (PV) solar panels are getting bigger applications in the practice. Their efficiency is better at lower temperatures. Normally the panels are cooled with the ambient air (in this case the gained heat is dissipated to the surrounding without any application). A successful combination of photovoltaic solar panel and solar collector is the so called photovoltaic-thermal (PV/T) solar panel. There are some significant advantages of the PV/T panels - aesthetic advantage over the PV panels, usage in places where the area is limited, reduction of the installation costs and architectural unity between roof and PV/T panels. The article analyses two solar panels - the PV solar panel of the type polycrystalline silicon (pc-Si) and the PV/T Solar Module CPVT60P250 (both solar panels are produced by the Crane Company using silicone cells from EKS - Solaris GmbH). Some tests are implemented and a comparison between the efficiencies of both panels is done.

Key words: combined photovoltaic/ thermal (PV/T) solar panel, photovoltaic solar panel, natural experiments, improved panel efficiency

Introduction

Solar photovoltaic-thermal panels (or PV/T panels) are a combination of photovoltaic cells and a solar thermal collector, i.e. they are a facility that turns solar radiation into electricity and heat at the same time. As a result PV-T panels generate more energy per unit area than a combination from individual PV (photovoltaic) panels and solar thermal collectors. Thus they present a new technology where the produced heat is some times more than the electricity.

There are some categorizations of the PV/T panels. The first one is after the fluid used in the panel (gas or liquid). The solar PV/T air panels are not so much used in the summer time because of the limited necessity of heat. The liquid PV/T panels have good applications mainly in the low-temperature range (starting by 10 to 80°C). They are used in different building installation as a coolant in evaporator circuits of "water to water" heat pumps (0 to 10 °C), in installation for heating of the pools (25 to 35 °C) and for production of domestic hot water and heating of buildings (not more than 60 °C) [1].

On the other side the liquid PV/T panels can be divide in two different panel types depending on the upper glass cover [2]. The glass-covered PV/T panels have higher electrical efficiency compared to the glazed panels. On the other side the glazed panels possess bigger thermal efficiency than the efficiency of the glass-covered PV/T panels. There is normally done a value's combination of the average thermal and electrical efficiency.

Simultaneous optimization of electrical and thermal efficiencies was done, too. It is presented by Mohsen in [3] - an experimental study and simulation of a solar photovoltaic thermal (PV/T) air collector was implemented. The results show (Figure 1) that electrical efficiency increase with 2.5 % at relative constant thermal efficiency (for example about 51.5%). Something similar happens with the thermal efficiency - it can be higher with about 2.5% at relative constant thermal efficiency (for example about 9.3%). This concept was developed by Vilfredo Pareto and is used as effectively from the engineering designers.

Two thin silicon film photovoltaic panels of type ASI®-F 32/12 for 12 V applications are presented in [4]. Cooling pipes are mounted on the back of the first solar panel converting it in PV/ T panel. The implemented experiments with both panels are described and their characteristics have been

compared. The results show that the electrical efficiency of the combined PV/ T panel is increased by about 3% compared with the standard one. Additionally - the heat output is 9 times greater than the corresponding electrical power.

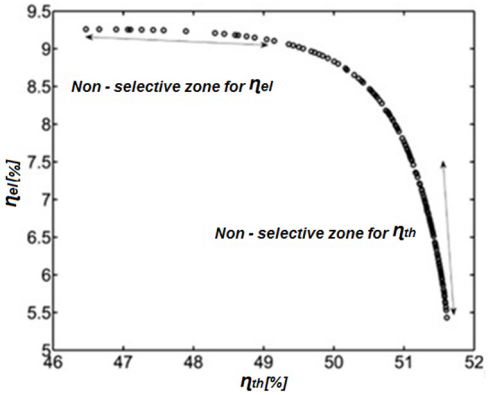

Figure 1– Optimization of thermal efficiency versus electrical efficiency of PV/T collector [3]

The aim of the present study is to perform tests with advanced PV and PV/T modules from polycrystalline silicon (pc-Si) produced by the company CRANE [5]. The experiments will be similar to the tests implemented in [4]. The solar panels have much greater electrical power - 250Wp. The electrical parameters of both panels are identical. The construction of the PV/T panel is designed as PV module with cooling pipes added to back side at the factory. The effect of the cooling pipes on the efficiency of the PV/ T panel, and the relationships between the heat flow rate and the produced electrical power will be investigated.

Test installation

The modules we use are of the following types [5]:

•PV solar panel of the type polycrystalline silicon (pc-Si) photovoltaic 250 Wp;

•PV/T Solar Module CPVT60P250 with rated electrical power of 250 Wp.

Suitable applications for the above mentioned solar panels are as follows [5]:

•Grid connected systems;

•Autonomous systems.

Another suitable application for the PV/T Solar Module CPVT60P250 should be the following [5]:

•Accessing to existing heating systems for homes and office buildings, heating pool water, or cooling by means of chillers.

Here is a list of the benefits for the combined PV/T panel [5]:

•Double effect – produce electricity and heat;

•Save space 1 module for 2 systems;

•Greatly improved paybacks over the combination of traditional PV & thermal technologies;

•Provides opportunities to most residential and light commercial low energy buildings to reach zero emission;

•Increase life of solar cells;

•Suitable for off-grid installation;

•Suitable with types off installation;

•Compact design;

•Low maintenance;

•Not necessary to enter cold water to reduce hazard of preheating of the water.

The typical uses of this module include 30.5 V stand-alone applications such as lighting systems, solar home systems, displays, light and guidance systems, telecommunications, driving systems (e.g. water-pump plants, gates), robots, and mobile applications (e.g. campers). Through the connection of higher system voltages, the modules are also excellently suited for the implementation of grid connected photovoltaic systems [5].

Some of the electrical data of both PV solar panel is shown in Table 1.

Table 1 – Electrical data of the PV solar panel of the type polycrystalline silicon (pc-Si) photovoltaic 250 Wp and solar module for 30.5 V applications CPVT60P250 [5]

Electrical data		
Parameter	**units**	**value**
Number of cells	-	60
Electrical power	Wp	250 -1 +3%
Voltage at maximum power	V	30.5
Open circuit voltage	V	37.8
Current at maximum	A	8.2
Short-circuit current	A	8.75
Efficiency	%	15.3
Working temperature range	ºC	-40 to 85
Maximal system voltage	V	1000
Rated diode current	A	20

The thermal data of the Solar Module for 30.5 V-Applications CPVT60P250 is shown in Table 2.

Table 2 – Thermal data of the Solar Module for 30.5 V-Applications CPVT60P250 [5]

Thermal data		
Parameter	**units**	**value**
Aperture area	m²	1.15
Thermal efficiency, η_0	%	55
Nominal heat flow rate	W	890
Volume flow rate	l/min	1.5 – 2.5
Flow losses	mm H_2O	540-880
Fluid volume	l	1.2
Effective thermal capacity	kJ/K	13.2

The main components of the installation are a combined PV/T solar panel and an ordinary photovoltaic solar panel (their pictures are shown in Figure 2). Some of the measurement elements are presented there, too. Both panels are oriented to the south with a slope of 40°.

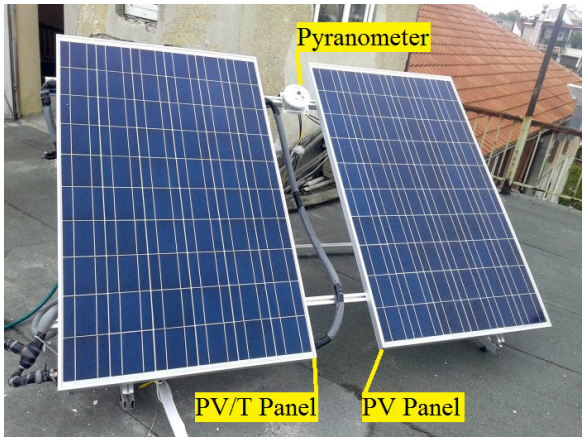

a)

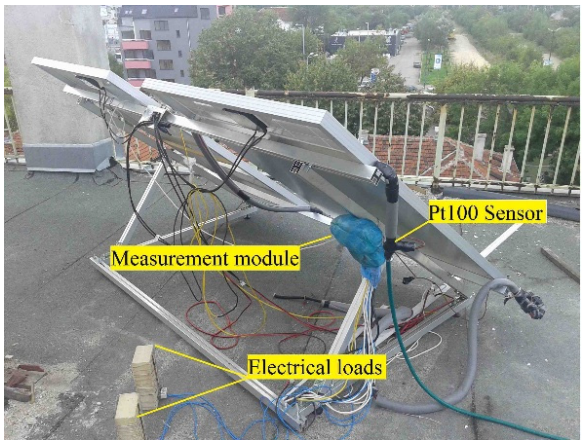

b)

Figure 2 –View of PV polycrystalline silicon (pc- Si) photovoltaic 250 Wp and PV/ T - CPVT60P250 panels: a) front view; b) back view

A sectional view of Solar Module CPVT60P250 is presented in Figure 3.

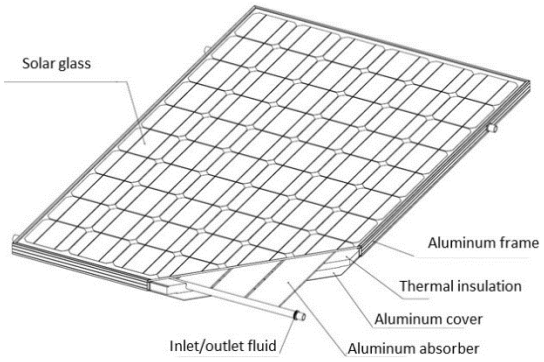

Figure 3 – Solar Module CPVT60P250 [5]

The experimental layout is shown in Figure 4.

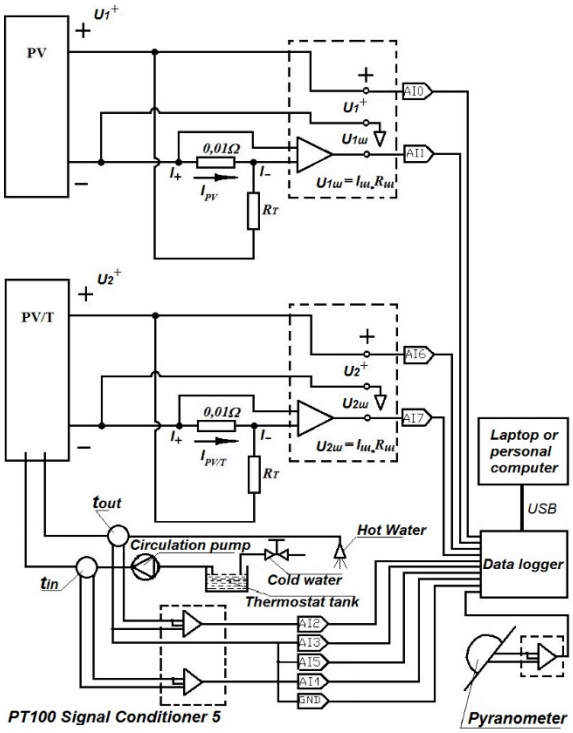

Figure 4 – Installation setup

A circulation pump is used to transport the cooling fluid through the combined panel and the thermostatic tank (it is used to maintain a constant fluid temperature in the PV/T panel circuit). PT100 sensors and signal conditioners are used to measure the inlet and outlet fluid temperatures in pipes. The signal is sent then to a data logger and treated by means of a Laptop or personal computer. Kipp & Zonen CMP6 pyranometer is mounted in the panel plane and is used to measure the global solar radiation.

The described installation is also used to measure the electrical power gained by both panels. For this purpose DC currents and voltages produced by the panels are measured. Two resistive loads (R_T) are connected in circuit by means to dissipate a produced electrical energy. The heat flow rate is determined, too. The main goal is to compare the electrical efficiencies of the two panels. The quantity of the gained thermal energy by the PV/T panel is calculated as well.

Experimental results

The experiment was carried out during 3 days – 16, 18 and 22 of August 2016. There were done 9 tests at different mean fluid temperatures (the mean value of inlet and outlet fluid temperature), inside the range of 25 - 60 °C. Each test had duration of about 20 min. The following parameters were measured: intensity of the global solar irradiation by means of pyranometer, ambient temperature, fluid flow rate, inlet and outlet fluid temperature trough the PV/T panel, produced electrical power by PV panel and produced electrical power by PV/T panel. The produced by PV/T panel heat flow rate, the ratio of electrical power produced by PV/T and PV panels, and the ratio of produced heat flow rate to electrical power by PV/T panel were calculated. All the mentioned parameters are shown in Table 3.

Table 3 – Test results

Parameter \ Test number	Test 1	Test 2	Test 3	Test 4	Test 5	Test 6	Test 7	Test 8	Test 9
Date	22.08.16	16.08.16	22.08.16	16.08.16	16.08.16	22.08.17	16.08.17	22.08.17	22.08.17
Start time, h	14:43	12:45	12:13	13:06	13:40	13:09	14:25	13:43	14:19
Intensity of the global solar radiation at the panel plane, W/m²	714	787	805,5	793	754	779,78	692,46	748	763
Ambient air temperature, °C	36,6	33,98	33,57	35,07	36,4	35,64	34,81	37,23	37,08
PV cell temperature, °C	61,1	65,37	62,1	63,6	65	60,6	59,47	60,5	59,78
Flow rate, l/min	2,1	1,55	2,3	2,3	2,3	2,3	2,3	2,3	2,3
Inlet fluid temperature, °C	22,97	26	31,71	33,63	37,9	41,6	44,8	51,06	60,5
Outlet fluid temperature, °C	28,55	29,98	34,61	35,4	40,1	43,25	46,01	51,6	60,1
Fluid temperature difference, °C	5,68	3,98	2,9	1,76	2,28	1,64	1,02	0,46	-0.36
Mean fluid temperature, °C	25,82	27,99	33,16	34,52	39	42,43	45,41	51,33	60,03
Produced electrical power (PV panel), W	164,55	181,66	180,4	181,7	174,5	172,44	168,88	170,2	168,9
Produced electrical power (PV/ T panel), W	166,73	183,36	182,93	184,48	175,4	174,5	167,5	168,73	164,64
Produced heat flow rate (PV/ T panel), W	557	262,02	313,6	191,34	247,4	175,15	129,7	49,6	-39,7
Ratio of produced electrical power by PV/ T panel and PV panel, %	101,32	101,49	101,4	101,53	100,52	101,19	99,18	99,14	97,48
Ratio of produced heat flow rate and electrical power by PV/T panel	3,38	1,59	1,74	1,05	1,42	1,02	0,77	0,29	-0,24

Some results from the test number 1 are presented in Figs.5 and 6. Figure 5 shows the produced electrical power by PV and PV/ T panels on 22.08.17 starting at 14:43 h. Figure 6 presents the produced electrical and heat flow rate by PV/ T panel during the same test. Some fluctuations of the produced electricity may be observed in Figure 5 due to the clouds. All values presented in Table 3 are averaged inside the measurement range, which is chosen carefully for each single test in case to overcome the transition mode (the starting part of the tests – first 19 min in Figure 5) and to calculate a steady state values. The transition mode is due to the large heat capacity of the panel that has been heated prior to the start of the fluid circulation through it. It is obviously that the cooled PV/T panel produces more electricity than the PV panel (Figure 6) in the steady state mode (selected measurement range – about 2,8 min long in Figure 6). Additionally the temperature of the cooling fluid increases which leads to thermal energy production. The ratio of produced heat flow rate and electrical power by PV/T

panel summarized for all nine tests is presented in Figure 7. The ratio of produced electrical power by PV/ T and PV panels is presented in Figure 8. Two trend lines have been fitted to experimental data and the equation polynomials are presented also in Figures.7 and 8 respectively.

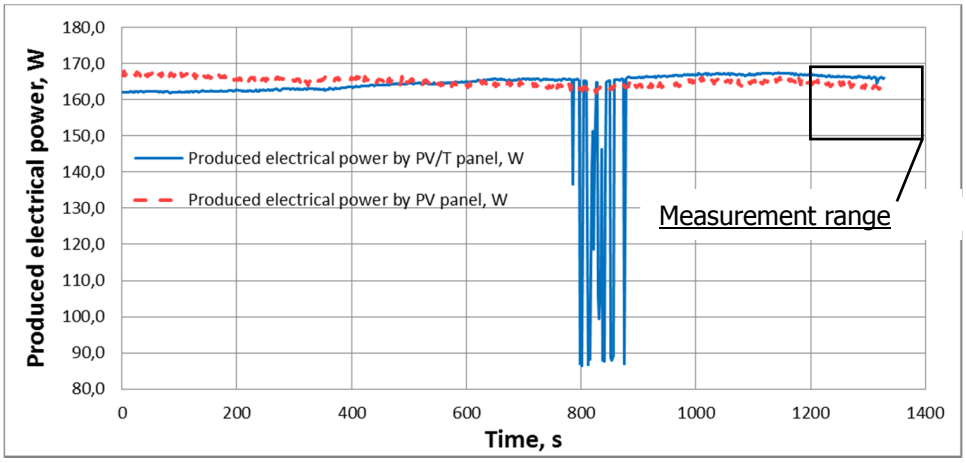

Figure 5 – Produced electrical power by PV and PV/ T panels at Test 1

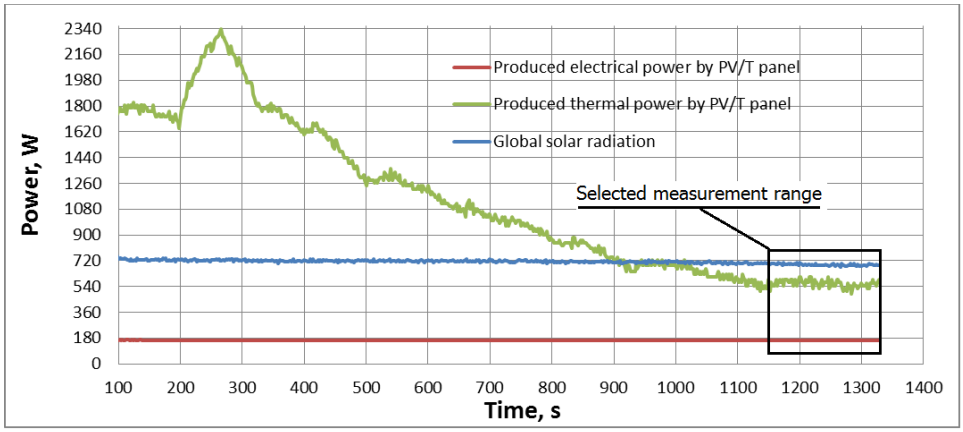

Figure 6 – Produced electrical power and heat flow rate by PV/ T panel at Test 1

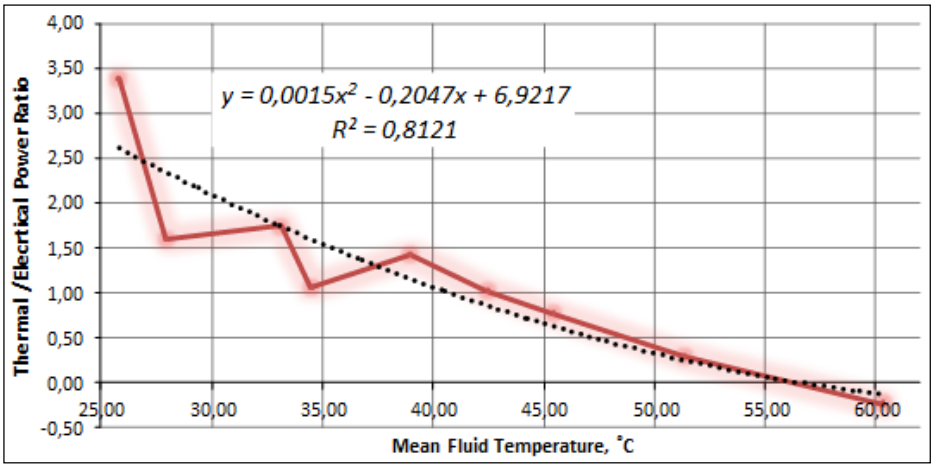

Figure 7 – Ratio of produced heat flow rate and electrical power by PV/ T panel

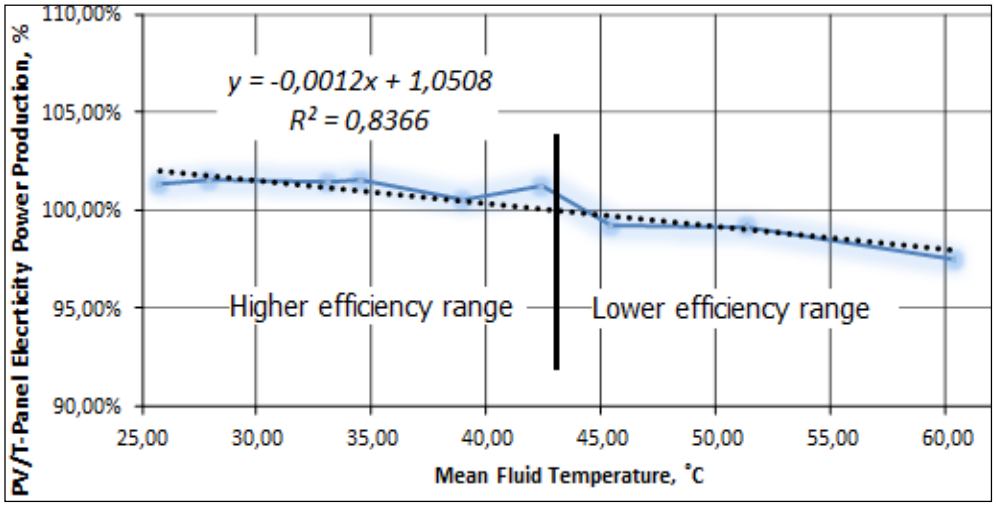

Figure 8 – Ratio of produced electrical power by PV/ T panel and PV panel vs. mean fluid temperature

Conclusion

An experimental work to measure the electrical power of two solar panels PV PV/T types is implemented. The following conclusions can be drawn on the base of the work done:

- the PV/T panel, when is more intensively cooled by means of a fluid, has higher efficiency than the other panel; this happens in the mean temperature range up to 43 °C (Figure 8 – Higher efficiency range);
- the PV panel, has higher efficiency than the PV/T panel at the mean fluid temperatures higher than 43 °C (Figure 8 – Lower efficiency range); this is due to better PV panel cooling by the ambient air in this range;
- the electrical power produced by PV/T panel is higher by 1.5% then the electrical power produced by PV panel at the mean fluid temperatures up to 35 °C;
- the production of thermal energy is relatively high (0,29-3,38 times more than the electrical power) in the whole working temperature range (from 20 till 60°C); than lower the working temperature of the panel is, so higher the gained heat flow rate becomes because of the higher heat transfer rate and lower heat losses (Table 2);
- a good stability of the produced electrical and thermal energy in a relatively large temperature interval is reported (Figure 8);
- compared to the earlier silicon thin film panel experiments described in [4], we have about a 2-times lower effect of efficiency gain on polycrystalline PV cells produced by CRANE using combined PV/T technology.

Acknowledgment

The author expresses the huge appreciation to Crane Ltd. Plovdiv, Bulgaria, (http://crane-bg.com/en) for the experimental and theoretical supports.

References

1 T. Matuska. Performance and economic analysis of hybrid PVT collectors in solar DHW system; SHC 2013. // International Conference on Solar Heating and Cooling for Buildings and Industry; – 2013. Freibur., Germany.

2 Jin-Hee Kim1., Jun-Tae Kim. Comparison of Electrical and Thermal Performances of Glazed and Unglazed PVT Collectors // Hindawi Publishing Corporation International Journal of Photoenergy Volumeю – 2012. – Article ID 957847. – P.7

3 M. M. Adeli., F. Sobhnamayan., S. Farahat. M., A. Alavi., F. Sarhaddi. Experimental Performance Evaluation of a Photovoltaic Thermal (PV/T) Air Collector and Its Optimization // Journal of Mechanical Engineering. – 2012. – Vol. 5. – P. 309-318.

4 A. Georgiev., R. Popov., I. Valkov., N. Kaloferov. Utilization of the thermal energy potential in photo voltaic solar panels // World Renewable Energy Congress XI 25. – 2010. Abu Dhabi. United Arab Emirates.

5 http://crane-bg.com

UDC 530.145; 530.12; 539.12-17

[1,2]Nurbakova G.S., [1,2]Habyl N., [2,3]Tyulemissov Zh.Zh.

[1]Physico-Technical Faculty, al-Farabi Kazakh National University, Almaty, Kazakhstan
[2]Scientific Research Institutes of Experimental and theoretical physics, Almaty, Kazakhstan
[3]Joint Institute for Nuclear Research, Dubna, Russia
e-mail: g.nurbakova@gmail.com

Strong form factor of delta (1232)

Abstract. Our article is devoted to study of the $\Delta \to N\pi$ decay. Strong decay $\Delta \to N\pi$ is one of the best modes to search for particles with spin 3/2. Strong decay is dominating channel of decay, i.e. Δ-isobar decay consist of 99% - hadronic decay, 1% - electromagnetic decay, therefore the decay is important for nuclear research. We calculate relevant form factors in the framework of the covariant quark model with infrared confinement in the full kinematical momentum transfer region. The covariant quark model has been applied to a large number of elementary particle processes. This model can be viewed as an effective quantum field approach to hadronic interactions, which based on an interaction Lagrangian of hadrons interacting with their constituent quarks. The coupling strength is determined by the compositeness condition $Z_{"} = 0$ where Z_H is the renormalization constant of the hadron wave function. We compare the obtained results with available experimental data and the results from other theoretical approaches.

Key words: relativistic quark model, confinement, Δ-isobar, strong decay, strong form factor.

Introduction

In hadron physics the strong interaction dominates the decay width of a resonance if appropriate hadronic channels are open. For Δ-isobar decay 99% - hadronic decay and 1% - electromagnetic decay.

The nucleon and the Δ-isobar are investigated as three-quark systems in the quark-confinement model (QCM). This model is based on two hypotheses. First, quark confinement is accomplished through averaging over some vacuum gluon fields which are assumed to provide the confinement of any colour states. Second, hadrons are treated as collective colourless excitations of quark-gluon interactions [1].

On the basis of nonlocal three-quark current of Δ-isobar and by using covariant confined quark model, we calculate mass operator (self-energy diagram), coupling constant and matrix element of $\Delta \to N\pi$ decay.

The covariant confined quark has been applied to a large number of elementary particle processes [4, 5]. This model can be viewed as an effective quantum field approach to hadronic interactions, which based on an interaction Lagrangian of hadrons interacting with their constituent quarks. The coupling strength is determined by the compositeness condition $Z_H = 0$ where Z_H is the renormalization constant of the hadron wave function. The hadron field renormalization constant Z_H characterizes the overlap between the bare hadron field and the bound state formed from the constituents. Once this constant is set to zero, the dynamics of hadron interactions is fully described by constituent quarks in quark loop diagrams with local constituent quark propagators. Matrix elements are generated by a set of quark loop diagrams according to the $1/N_c$ expansion. The ultraviolet divergences of the quark loops are regularized by including vertex functions for the hadron-quark vertices which, in addition, describe finite size effects due to the non-pointlike structure of hadrons. Quark confinement was implemented into the model [6] by introducing an infrared cutoff on the upper limit of the scale integration to avoid the appearance of singularities in any matrix element. The infrared cutoff parameter λ is taken to have a common value for all processes. The covariant confined quark model contains only a few model parameters: the light and heavy constituent quark masses, the size parameters that describe the size of the distribution of the constituent quarks inside the hadrons and the infrared cutoff parameter λ. They are determined by a fit to available experimental data.

Effective Lagrangian

The coupling of a Δ-isobar to its constituent quarks q_1, q_2 and q_3 is described by the Lagrangian

$$L_{\Delta}(x) = ig_{\Delta}\bar{\Delta}^{k_1k_2k_3}_{\mu\alpha}(x)(J^{\mu\alpha})^{k_1k_2k_3}(x) + h.c. \quad (1)$$

where

$$(J^{\mu\alpha}_{3q})^{k_1k_2k_3}(x) = \iiint dx_1dx_2dx_3F_{\Delta}(x;x_1,x_2,x_3)(J^{\mu\alpha}_{3q})^{k_1k_2k_3}(x_1,x_2,x_3) \quad (2)$$

$$(J^{\mu\alpha}_{3q})^{k_1k_2k_3}(x_1,x_2,x_3) = \varepsilon^{a_1a_2a_3}\Gamma^{\mu}_{\alpha;\alpha_1,\alpha_2,\alpha_3}q^{k_1}_{a_1\alpha_1}(x_1)q^{k_2}_{a_2\alpha_2}(x_2)q^{k_3}_{a_3\alpha_3}(x_3),$$

here,

$$\Gamma^{\mu}_{\alpha;\alpha_1,\alpha_2,\alpha_3} = (\Gamma_1)_{\alpha\alpha_1}\otimes(\Gamma^{\mu}_2)_{\alpha_2\alpha_3} = (I)_{\alpha\alpha_1}\otimes(C\gamma^{\mu})_{\alpha_2\alpha_3} - \frac{i}{2}(\gamma_{\nu})_{\alpha\alpha_1}\otimes(C\sigma^{\mu\nu})_{\alpha_2\alpha_3}$$

is a Dirac matrix which projects onto the spin quantum number of the isobar field. The function F_{Δ} is characterizes the finite size of the isobar. To satisfy translational invariance the function F_{Δ} has to fulfill the identity $F_{\Delta}(x + a; x_1 + a, x_2 + a, x_3 + a) = F_{\Delta}(x; x_1, x_2, x_3)$ for any four-vector $\boldsymbol{a}$. In the following we use a specific form for the scalar vertex function

$$F_{\Delta}(x;x_1,x_2,x_3) = \delta\left(x - \sum_{i=1}^{3}x_i\omega_i\right)\Phi_{\Delta}\left(\sum_{i<j}\left(x_i - x_j\right)^2\right), \quad (3)$$

where Φ_M is the correlation function of the constituent quarks with masses m_{q_1}, m_{q_2}, m_{q_3} and the mass ratios $\omega_i = m_{q_i}/(m_{q_1} + m_{q_2} + m_{q_3})$.

We choose a simple Gaussian form of the vertex function $\widetilde{\Phi}_{\Delta}(-k^2)$. The minus sign in the argument of this function is chosen to emphasize that we are working in the Minkowski space. One has

$$\widetilde{\Phi}_{\Delta}(-k^2) = exp\left(k^2/\Lambda^2_{\Delta}\right) \quad (4)$$

where the parameter Λ_{Δ} characterizes the size of the meson. Since k^2 turns into $-k^2_E$ in the Euclidean space, the form (4) has the appropriate fall-off behavior in the Euclidean region. We emphasize that any choice for Φ_M is appropriate as long as it falls off sufficiently fast in the ultraviolet region of the Euclidean space to render the corresponding Feynman diagrams ultraviolet finite. We choose a Gaussian form for Φ_M for calculation convenience.

Strong form factors of Δ(1232) in the covariant quark model

We will study strong decay of Δ^{++} to proton and positive pion to investigate the strong form factors of Δ(1232).

The matrix element corresponding to that Feynman diagram represented as

$$M(\Delta \to p\pi) = g_{\Delta}g_pg_{\pi}\int dx\int dy\int dz\cdot e^{ip'x-ipy+iqz}\times$$
$$\times\bar{u}_p(p')\left\langle 0\left|T\left\{J_p(x)\bar{J}^{\mu}_{\Delta}(y)J_{\pi}(z)\right\}\right|0\right\rangle u^{\mu}_{\Delta}(p), \quad (5)$$

The Feynman diagram which describes this process is given in Figure 1.

Three-quarks current of proton and pion given in similar way with Δ-isobar,

$$J_p(x) = \int dx_1dx_2dx_3F_N(x;x_1,x_2,x_3)J_{3q}(x_1,x_2,x_3),$$
$$J_{3q}(x_1,x_2,x_3) = \quad (6)$$
$$= \Gamma^A\gamma^5d^{a_1}(x_1)\left[\varepsilon^{a_1a_2a_3}u^{a_2}(x_2)C\Gamma_Au^{a_3}(x_3)\right],$$

$$J_{\pi}(z) = \int dz_1dz_2F_{\pi}(z;z_1,z_2)J_{3q}(z_1,z_2),$$
$$J_{3q}(z_1,z_2) = \bar{d}(z_1)i\gamma^5u(z_2).$$

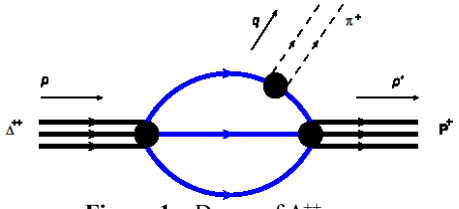

Figure 1 – Decay of $\Delta^{++}\to p\pi$

The matrix $C=\gamma^0\gamma^2$ is the usual charge conjugation matrix and the a_i (i = 1, 2, 3) are color indices. There are two possible kinds of nonderivative three-quark currents: $\Gamma^A \otimes \Gamma_A = \gamma^\alpha \otimes \gamma_\alpha$ (vector current) and $\Gamma^A \otimes \Gamma_A = 1/2\ \sigma^{\alpha\beta} \otimes \sigma_{\alpha\beta}$ (tensor current) with $\sigma^{\alpha\beta} = i/2\ (\gamma^\alpha\gamma^\beta - \gamma^\beta\gamma^\alpha)$.

Let us write the T-production for the matrix element in eq.(5)

$$\left\langle 0\left|T\left\{J_p(x)\bar{J}^{\mu}_{\Delta}(y)J_{\pi}(z)\right\}\right|0\right\rangle = 12\Gamma^A\gamma^5 S_d(x_1-z_1)i\gamma_5 S_u(z_2-y_1)\Gamma_1\cdot tr\left[S_u(y_2-x_2)\Gamma_A S_u(x_3-y_3)\Gamma_2^{\mu}\right]+$$
$$+24\Gamma^A\gamma^5 S_d(x_1-z_1)i\gamma_5 S_u(z_2-y_1)\Gamma_2^{\mu} S_u(y_2-x_2)\Gamma_A S_u(x_3-y_3)\Gamma_1$$

Then we rewrite the M-martix as

$$M(\Delta\to p\pi) = 12ig_\Delta g_p g_\pi \int dx\int dy\int dz e^{ip'x-ipy+iqz}\int dx_1dx_2dx_3\delta\left(x-\sum_{i=1}^{3}x_iv_i\right)\Phi_p\left[\sum_{i<j}(x_i-x_j)^2\right]$$
$$\int dy_1dy_2dy_3\delta\left(y-\sum_{i=1}^{3}y_iw_i\right)\Phi_p\left[\sum_{i<j}(y_i-y_j)^2\right]\int dz_1dz_2\delta\left(z-\sum_{i=1}^{2}z_i\eta_i\right)\Phi_\pi\left[\sum_{i<j}(z_1-z_2)^2\right]$$
$$\bar{u}_p(p')\begin{Bmatrix}\Gamma^A\gamma^5 S_d(x_1-z_1)\gamma_5 S_u(z_2-y_1)\Gamma_1\cdot tr\left[S_u(y_2-x_2)\Gamma_A S_u(x_3-y_3)\Gamma_2^{\mu}\right]\\ +2\Gamma^A\gamma^5 S_d(x_1-z_1)\gamma_5 S_u(z_2-y_1)\Gamma_2^{\mu} S_u(y_2-x_2)\Gamma_A S_u(x_3-y_3)\Gamma\end{Bmatrix}u^{\mu}_{\Delta}(p)$$
$$\int dx\int dy\int d\rho_1^x\int d\rho_2^x\int d\rho_1^y\int d\rho_2^y\int dz_1\int dz_2$$
$$\times\exp\begin{bmatrix}ip'x-ipy+iq(\eta_1z_1+\eta_2z_2)-i\omega_1^x\rho_1^x-i\omega_2^x\rho_2^x-i\omega_1^y\rho_1^y-i\omega_2^y\rho_2^y-il(z_1-z_2)\\ -ik_1(x_1-z_1)-ik_1(z_2-y_1)-ik_3(y_2-z_2)-ik_4(z_3-y_3)\end{bmatrix}$$

After integrating by space coordinates we get a set of δ-functions, which help us to vanish some momentum integrations. As a result we have

$$M(\Delta^{++}\to p\pi) = (2\pi)^4 i\delta(p-p'-q)T(\Delta^{++}\to p\pi^+)$$

where

$$T(\Delta^{++}\to p\pi^+) = -12g_\Delta g_p g_\pi\int\frac{d^4k_1}{(2\pi)^4 i}\int\frac{d^4k_2}{(2\pi)^4 i}\tilde{\Phi}_p\left[-\omega_x^2\right]\tilde{\Phi}_\Delta\left[-\omega_y^2\right]\tilde{\Phi}_p\left[-(k_1-\eta_2q)^2\right]$$
$$\bar{u}_p(p')\begin{Bmatrix}\Gamma^A\gamma^5 S_d(k_1-q)\gamma_5 S_u(k_1)\Gamma_1\cdot tr\left[S_u(k_2)\Gamma_A S_u(k_2-k_1+p)\Gamma_2^{\mu}\right]\\ +2\Gamma^A\gamma^5 S_d(k_1-q)\gamma_5 S_u(k_1)\Gamma_2^{\mu} S_u(k_2)\Gamma_A S_u(k_2-k_1+p)\Gamma_1\end{Bmatrix}u^{\mu}_{\Delta}(p) =$$
$$= G_{\Delta p\pi}\cdot p'_{\mu}\cdot\bar{u}_p(p',\lambda')u^{\mu}_{\Delta}(p,\lambda)$$

We use the next definitions

$$\begin{cases}\omega_1^x = \frac{1}{\sqrt{2}}\left[-k_1+k_3+p-v_3p'\right]\\ \omega_2^x = \frac{1}{\sqrt{6}}\left[k_1+k_3-p+(2v_2+v_3)p'\right]\end{cases},\quad\begin{cases}\omega_1^y = \frac{1}{\sqrt{2}}\left[k_1-k_3-(\omega_1+\omega_2)p\right]\\ \omega_2^y = \frac{1}{\sqrt{6}}\left[-k_1-k_3+(\omega_1-\omega_2)p\right]\end{cases}$$

After loop integration we get 4-integral, which are numerically calculated. It is convenient to approximate the result of numerical calculations by dipole function

$$G(Q^2)=\frac{1}{\left[1+Q^2/\Lambda_D^2\right]^2}$$

where, parameter $\Lambda_D = 0.96$ GeV. Function behavior in the region $0 \le Q^2 = -q^2 \le 2.5$ GeV^2 represented at Figure 2.

For comparison we use graphics from others theoretical approaches such as [1]-[3] and results of lattice QCD calculations [4]. For graphic 3 we use parameterization given in work [2]

$$G(\vec{q}^{\,2})=\frac{1}{\left[1+\vec{q}^{\,2}/\lambda_1^2+\vec{q}^{\,4}/\lambda_2^4\right]}$$

where $\lambda_1 = 0.594$ GeV, $\lambda_2 = 0.998$ GeV. $\vec{q}^{\,2} = q_0^2 + Q^2$.

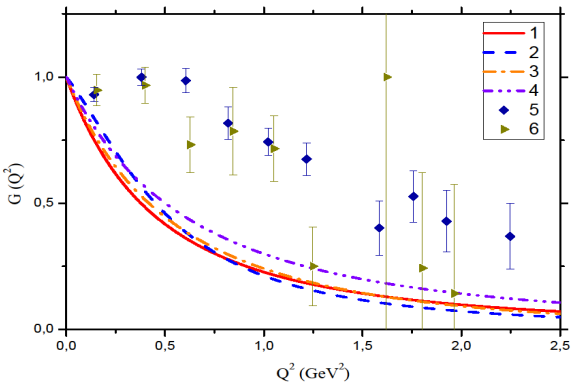

Figure 2 – Strong form factor of Δ-isobar

Also we represent Table 1 with numerical values of strong coupling constants $G_{\Delta p\pi}$.

Table 1 – Strong constant of decay

	Exp	Our work	[1]	[2]	[3]	[5]	[6]	[7]	[8]
$G_{\Delta p\pi}[GeV^{-1}]$	15.4±2.9	15.2	17.0	11.14	14.98	14.85	17.76	15.2	13.4±5.4

Conclusion

We calculate coupling constant of delta-isobar. The calculated value of coupling constant is in good agreement with the experimental data.

We built the graphic of $G(Q^2)$ in Euclidian region of squared momentum transfer $Q^2=-q^2$. We compare our results with [1]-[3], [5]-[8] works. Our results are close to work [2].

Acknowledgment

This work was supported by the Ministry of Education and Science of the Republic of Kazakhstan, Grant "The BT of HEI"(2016) and Grant No. 3091/GF4, state registration No. 0115RK01041.

References

1. G.V. Efimov., M. A. Ivanov., V. E. Lyubovitskij. Strong Nucleon and Δ–Isobar Form Factors in the Quark Confinement Model. // Few Body Syst. – 1989. – Vol.6. – P. 17-43.

2. T. Melde., L. Canton. W. Plessas. Structure of meson–baryon interaction vertices // Phys. Rev. Lett. – 2009. – Vol. 102. – P. 625.

3. V. Mader., G. Eichmann., M. Blank., A. Krassnigg. Hadronic decays of mesons and baryons in the Dyson-Schwinger approach // Phys. Rev. D. – 2011. – Vol. 84. – P. 034012.

4. C. Alexandrou., G. Koutsou., J. W. Negele., Y. Proestos., A. Tsapalis. Nucleon to Delta transition form factors with NF = 2 + 1 domain wall fermions // Phys. Rev. D. – 2011. – Vol.83. – P. 014501.

5. T. Sato., T. S. H. Lee. Meson exchange model for πN scattering and gamma N → πN reaction // Phys. Rev. C. – 1996. – Vol. 54. – P. 2600

6. H. Polinder., T. A. Rijken., Soft–core meson–baryon interactions. II. πN and K^+N scattering // Phys. Rev. C. – 2005. – Vol. 72. – P. 065210.

7. J. A. Niskanen. The πNΔcoupling and the Δ (1232) resonance width // Phys. Lett. B. – 1981. – Vol. 107. – P. 344.

8. Z. Wang. Strong decay Δ++ → pπ with light–cone QCD sum rules // Eur. Phys. J. – 2008. – C. 57. – P. 711–718.

UDC 530.145; 530.12; 539.12-17

[1,2*]Nurbakova G.S., [3]Ivanov M.A., [1,2]Habyl N., [2,3]Tyulemissov Zh.Zh., [3,4]Tyulemissova A.

[1]Physico-Technical Faculty, al-Farabi Kazakh National University, Almaty, Kazakhstan
[2]Scientific Research Institutes of Experimental and theoretical physics, Almaty, Kazakhstan
[3]Joint Institute for Nuclear Research, Dubna, Russia
[4]Dubna University, Dubna, Russia
[*]e-mail: g.nurbakova@gmail.com

The three quark-current of delta-isobar

Abstract. Strong decay $\Delta \to N\pi$ is one of the best modes to search for particles with spin 3/2. Δ-isobar decay consist of 99% - hadronic decay and 1% - electromagnetic decay, i.e. in this process strong decay is dominating channel which makes it important for nuclear research. The relativistic three-quark current describe all parameters of particle in quantum field theory. The three-quark current of Delta-isobar is similar with all large group of particles with quantum numbers $J^P=(3/2)^+$. Relevant interpolating three-quark current is given in great details. It is shown that, this current has a single form. If we have three-quark current, we can write the interaction Lagrangian of baryon interacting with their constituent quarks. The Lagrangian is the base of the Standard model. The generalization of the current to nonlocal case can be used to such nonlocal theory as covariant quark model. Covariant quark model has been applied to a large number of elementary particle processes.

Key words: covariant quark model, confinement, Δ-isobar, relativistic three-quark current.

Introduction

On LHCb at 14 march 2017 was published preprint about discovery of $\Omega_c(3000)^0$, $\Omega_c(3050)^0$, $\Omega_c(3066)^0$, $\Omega_c(3090)^0$ and $\Omega_c(3119)$ that gave an impetus for study of Ω_c-baryon [1]. Therefore, we need to construct the relativistic three-quark current of particles with quantum numbers $J^P=(3/2)^+$. Since we have not any physical quantities, we started from reference decay $\Delta \to N\pi$ and wrote the corresponding three-quark current [2]. Strong decay $\Delta \to N\pi$ is one of the best modes to search for particles with spin 3/2. Δ-isobar decay consist of 99% - hadronic decay and 1% - electromagnetic decay, i.e. in this process strong decay is dominating channel which makes it important for nuclear research.

The relativistic three-quark current describe all parameters of particle in quantum field theory. The three-quark current of Delta-isobar is similar with all large group of particles with quantum numbers $J^P=(3/2)^+$.

At first we needed to construct relevant interpolating three-quark current. For this purpose we use Rarita-Schwinger equation, properties of Delta-isobar and Fierz transformation. It is shown that the current has a single form. If we know the Δ-isobar current, we can write an interaction Lagrangian of baryon with their constituent quarks. The Lagrangian is the base of the Standard model. The generalization of the current to nonlocal case can be used to such nonlocal theory as covariant quark model. Covariant quark model has been applied to a large number of elementary particle processes.

The three quark-current of delta-isobar

The relevant interpolating three-quark current with quantum numbers $J^P = (3/2)^+$ is given

$$\left(J^{\mu}\right)^{k_1k_2k_3} = \varepsilon^{a_1a_2a_3}\Gamma_1 q_{a_1}^{k_1}\left[\left(q_{a_2}^{k_2}\right)^T C\Gamma_2 q_{a_3}^{k_3}\right], \qquad (1)$$

where $a_1, a_2, a_3 = 1,2,3$ are the color indeces; C is the charge conjugation matrix; $1\,k_1, k_2, k_3 = 1,2$ are isospin indeces. We did not write the Lorenz index "μ" down clearly, because it can be either in Γ_1 or in Γ_2.

The charge conjugation matrix have following properties

$$C = C^{-1} = C^{+} = -C^{T}$$

We will use properties given by

$$C\Gamma^T C^{-1} = \begin{cases} \Gamma, & for\ \Gamma = S, P, A \\ -\Gamma, & for\ \Gamma = V, T \end{cases}. \qquad (2)$$

where $S \to I, P \to \gamma^5, A \to \gamma^\mu\gamma_5, T \to \sigma^{\mu\nu}$.

Table 1 – The two quark color state $\left(q_{a_2}^{k_2}\right)^T C\Gamma_2 q_{a_3}^{k_3}\varepsilon^{a_1a_2a_3}$ is diquark

The scalar diquark	$\left(q_{a_2}^{k_2}\right)^T C\gamma_5 q_{a_3}^{k_3}\varepsilon^{a_1a_2a_3}$	$J^P=0^+$
The pseudoscalar diquark	$\left(q_{a_2}^{k_2}\right)^T C q_{a_3}^{k_3}\varepsilon^{a_1a_2a_3}$	$J^P=0^-$
The vector diquark	$\left(q_{a_2}^{k_2}\right)^T C\gamma_5\gamma^5 q_{a_3}^{k_3}\varepsilon^{a_1a_2a_3}$	$J^P=1^-$
The axial-vector diquark	$\left(q_{a_2}^{k_2}\right)^T C\gamma^\mu q_{a_3}^{k_3}\varepsilon^{a_1a_2a_3}$	$J^P=1^+$
The tensor diquark	$\left(q_{a_2}^{k_2}\right)^T C\gamma_5\sigma^{\mu\nu} q_{a_3}^{k_3}\varepsilon^{a_1a_2a_3}$	$J^P=1_+$
The pseudotensor diquark	$\left(q_{a_2}^{k_2}\right)^T C\sigma^{\mu\nu} q_{a_3}^{k_3}\varepsilon^{a_1a_2a_3}$	$J^P=1^-$

where $\sigma^{\mu\nu} = i/2\left[\gamma^\mu,\gamma^\nu\right]$.

The multiplet of all isospin states of Delta-isobar is $\Delta^{k_1k_2k_3}(x)$. The spinor $\Delta^{k_1k_2k_3}$ is symmetric under permutation of k_1,k_2,k_3 and obey the Rarita-Schwinger equation $\Delta_\mu\gamma^\mu = 0$ and $\partial_\mu\gamma^\mu = 0$. Connection of multiplet elements to physical conditions are

$$\Delta^{111} = \Delta^{++}, \quad \Delta^{211} = \frac{1}{\sqrt{3}}\Delta^+, \quad \Delta^{122} = \frac{1}{\sqrt{3}}\Delta^0, \quad \Delta^{222} = \Delta^- \tag{3}$$

Since there is a symmetry in an arbitrary permutation of the indices of the isospin indices in the spinor $\Delta^{k_1k_2k_3}$, the corresponding three-quark current also has this property. This means that the current in Eq. (1) must be symmetric under a permutation of $k_1 \leftrightarrow k_2 \leftrightarrow k_3$.This condition imposes restrictions on the choice of matrices. First we consider a permutation of the indices in the diquark. Equity must be satisfied

$$\varepsilon^{a_1a_2a_3} q_{a_2\alpha_2}^{k_2}\left(C\Gamma_2\right)_{\alpha_2\alpha_3} q_{a_3\alpha_3}^{k_3} = \varepsilon^{a_1a_2a_3} q_{a_2\alpha_2}^{k_3}\left(C\Gamma_2\right)_{\alpha_2\alpha_3} q_{a_3\alpha_3}^{k_2}. \tag{4}$$

Taking into account the anticommutativity of the fermions fields, we swap the quarks on the right-hand side of the equation. Thus we have the following equation:

$$\varepsilon^{a_1a_2a_3} q_{a_3\alpha_3}^{k_3}\left(C\Gamma_2\right)_{\alpha_2\alpha_3} q_{a_2\alpha_2}^{k_2} = -\varepsilon^{a_1a_2a_3} q_{a_3\alpha_3}^{k_2}\left(C\Gamma_2\right)_{\alpha_2\alpha_3} q_{a_2\alpha_2}^{k_3} = \varepsilon^{a_1a_2a_3} q_{a_2\alpha_3}^{k_2}\left(C\Gamma_2\right)^T_{\alpha_3\alpha_2} q_{a_3\alpha_2}^{k_3}. \tag{5}$$

We see that right-hand side and left-hand side of Eq. (0.1) is equal for

$$C\Gamma_2 = \left(C\Gamma_2\right)^T = \Gamma_2^T C^T = -\Gamma_2^T C, \quad C\Gamma_2^T C^{-1} = -\Gamma_2. \tag{6}$$

From Eq. (2) Γ_2 may be either vector $\Gamma_2 = \gamma^\mu$ or tensor $\Gamma_2 = \sigma^{\mu\nu}$. It is known that Δ-isobar has positive parity. Consider the case of $\Gamma_2 = \gamma^\mu$ corresponding to axial-vector diquark (Table 1) with positive parity, hence $\Gamma_1 = I$. In the case of $\Gamma_2 = \sigma^{\mu\nu}$ it follows that $\Gamma_1 = \gamma_\nu$.

Let us consider the case of interchanging of k_1 and k_2. In this case, we have following identity

$$\varepsilon^{a_1a_2a_3}\left(\Gamma_1\right)_{\alpha\alpha_1} q_{a_1\alpha_1}^{k_1}\cdot\left[q_{a_2\alpha_2}^{k_2}\left(C\Gamma_2\right)_{a_2\alpha_3} q_{a_3\alpha_3}^{k_3}\right] = \varepsilon^{a_1a_2a_3}\left(\Gamma_1\right)_{\alpha\alpha_1} q_{a_1\alpha_1}^{k_1}\cdot\left[q_{a_2\alpha_2}^{k_2}\left(C\Gamma_2\right)_{a_2\alpha_3} q_{a_3\alpha_3}^{k_1}\right]. \tag{7}$$

One can interchange q^{k_1} and q^{k_3} quarks in right-hand side of identity. Thus we have

$$-\varepsilon^{a_1a_2a_3}\left(\Gamma_1\right)_{\alpha\alpha_1} q^{k_1}_{a_3\alpha_3}\cdot\left[q^{k_2}_{a_2\alpha_2}\left(C\Gamma_2\right)_{a_2\alpha_3} q^{k_3}_{a_1\alpha_1}\right]= \\ =\varepsilon^{a_3a_2a_1}\left(\Gamma_1\right)_{\alpha\alpha_1} q^{k_1}_{a_1\alpha_1}\cdot q^{k_1}_{a_3\alpha_3}\cdot\left[q^{k_2}_{a_2\alpha_2} C_{\alpha_2\beta_2}\left(\Gamma_2\right)_{\beta_2\alpha_3} q^{k_3}_{a_1\alpha_1}\right]. \quad (8)$$

Next use Fierz transformation

$$4\left(\Gamma_1\right)_{\alpha\alpha_1}\left(\Gamma_2\right)_{\beta_2\alpha_3}=\sum_D\left(\Gamma_1\Gamma^D\right)_{\alpha\alpha_3}\left(\Gamma_2\Gamma^D\right)_{\beta_2\alpha_1}. \quad (9)$$

where $\Gamma^D=\left\{I,\gamma^\mu,\sigma^{\mu\nu}\left(\mu<\nu\right),\gamma^5,i\gamma^\mu\gamma_5\right\}$ is complete set of the base Dirac matrix.

First we introduce some notation.

$$\begin{cases}\left(O_1\right)_{\alpha\alpha_1}\left(O_2\right)_{\beta_2\alpha_3}=\left(\tilde{O}_1\right)\otimes\left(\tilde{O}_2\right)\\ \left(O_1\right)_{\alpha\alpha_3}\left(O_2\right)_{\beta_2\alpha_1}=\left(O_1\right)\otimes\left(O_2\right)\end{cases} \quad (10)$$

We have two combination of gamma matrix

$$\Gamma_1\times\Gamma_2=I\times\gamma^\mu. \quad (11)$$

$$\Gamma_1\times\Gamma_2=\gamma_\nu\times\sigma^{\mu\nu}. \quad (12)$$

We will first discuss the case of $\Gamma_1\times\Gamma_2=I\times\gamma^\mu$. Thus we obtain

$$4\tilde{I}\otimes\tilde{\gamma}^\mu=I\otimes\gamma^\mu+\gamma_\alpha\otimes\gamma^\mu\gamma^\alpha+ \\ +\frac{1}{2}\sigma_{\alpha\beta}\otimes\gamma^\mu\sigma^{\alpha\beta}+\gamma_5\otimes\gamma^\mu\gamma_5-\gamma_\alpha\gamma_5\otimes\gamma^\mu\gamma^\alpha\gamma_5 \quad (13)$$

The right-hand side of identity can be transformed to basis by using the following expression

$$\gamma_5\sigma^{\mu\nu}=-\frac{i}{2}\varepsilon^{\mu\nu\alpha\beta}\sigma_{\alpha\beta}, \quad (14)$$

where we use Levi-Civita symbol presented as $\varepsilon_{0123}=-\varepsilon^{0123}=1$.

After long transformation one can obtain

$$4\tilde{I}\otimes\tilde{\gamma}^\mu=I\otimes\gamma^\mu+\gamma^\mu\otimes I-i\gamma_\nu\otimes\sigma^{\mu\nu}+ \\ +i\sigma^{\mu\nu}\otimes\gamma_\nu+i\sigma^{\mu\nu}\gamma_5\otimes\gamma_\nu\gamma_5+\gamma_5\otimes\gamma^\mu\gamma_5 \\ -\gamma^\mu\gamma_5\otimes\gamma_5+i\gamma_\nu\gamma_5\otimes\sigma^{\mu\nu}\gamma_5. \quad (15)$$

Transformations of Eq. (0.2) will also take place in a similar manner, we find that

$$4\tilde{\gamma}_\nu\otimes\tilde{\sigma}^{\mu\nu}=i\left(3I\otimes\gamma^\mu-3\gamma^\mu\otimes I+i\gamma_\nu\otimes\sigma^{\mu\nu}+i\sigma^{\mu\nu}\otimes\gamma_\nu-i\sigma^{\mu\nu}\gamma_5\otimes\gamma_\nu\gamma_5-3\gamma_5\otimes\gamma^\mu\gamma_5-3\gamma^\mu\gamma_5\otimes\gamma_5+i\gamma_\nu\gamma_5\otimes\sigma^{\mu\nu}\gamma_5\right). \quad (16)$$

The symmetry with respect to permutation of indeces $k_2\leftrightarrow k_3$, to Rarita-Schwinger equation $\bar{\Delta}^\mu\gamma_\mu=0$ and to the identity

$$i\gamma_\nu\gamma_5\otimes\sigma^{\mu\nu}\gamma_5=-i\gamma_\nu\otimes\sigma^{\mu\nu}, \quad (17)$$

leads to the relation

$$\begin{cases}4\tilde{I}\otimes\tilde{\gamma}^\mu=2I\otimes\gamma^\mu-2i\gamma_\nu\otimes\sigma^{\mu\nu}\\ 4i\tilde{\gamma}_\nu\otimes\tilde{\sigma}^{\mu\nu}=-4I\otimes\gamma^\mu\end{cases} \quad (18)$$

It is clear that combination

$$\Gamma_1\otimes\Gamma_2=I\otimes\gamma^\mu-\frac{i}{2}\gamma_\nu\otimes\sigma^{\mu\nu}, \quad (19)$$

is symmetric under Fierz transformation and transform in itself. Thus, three-quark current of Δ-isobar has only possible form

$$\left(J^\mu\right)^{k_1k_2k_3}=\varepsilon^{a_1a_2a_3} \\ \left[q^{k_1}_{a_1}\cdot\left[q^{k_2}_{a_2}C\gamma^\mu q^{k_3}_{a_3}\right]-\frac{i}{2}\gamma_\nu q^{k_1}_{a_1}\cdot\left[q^{k_2}_{a_2}C\sigma^{\mu\nu}q^{k_3}_{a_3}\right]\right]. \quad (20)$$

Conclusion

We construct the relativistic three-quark current of Delta-isobar. For this, we use the nontrivial way from permutation invariance and parity invariance. Rarita-Schwinger equation and Fierz transformation enabled to construct the symmetric three-quark current under isospin indices permutations.

The generalization of the Delta-isobar current to nonlocal cases enables to describe any of large group of particles, such as $\Omega_c(3000)^0$, $\Omega_c(3050)^0$, $\Omega_c(3066)^0$, $\Omega_c(3090)^0$, $\Omega_c(3119)$ and others with quantum numbers $J^p=(3/2)^+$.

Acknowledgment

This work was supported by the Ministry of Education and Science of the Republic of Kazakhstan, Grant "The BT of HEI"(2016) and Grant No. 3091/GF4, state registration No. 0115RK01041.

References

1. LHCb Collaboration. Observation of five new narrow Ω_c states decaying to $\Xi_c^+K^-$ //arXiv:1703.04639 [hep-ex].

2. G.V. Efimov., M.A. Ivanov., V.E. Lyubovitskij. Strong Nucleon and Δ-Isobar Form Factors in the Quark Confinement Model // Few Body Syst. – 1989. – Vol. 6. – P. 17-43.

UDK 535:530.182

*Davletov A.E., Kudyshev Zh.A., Mukhametkarimov Ye.S., Kissan A., Yerimbetova L.T.
Department of Plasma Physics, al-Farabi Kazakh National University,
Tole Bi 96, Almaty 050012, Kazakhstan
*e-mail:askar@physics.kz

Dispersion of electromagnetic waves in layered graphene-dielectric metamaterials

Abstract. In this paper possibility of creating a medium based on graphene-dielectric (quartz) structures with a hyperbolic shape of the dispersion relation is considered. Using the Bloch theorem and the transfer matrix method, dispersion relations are found for hyperbolic media, consisting of periodically located layers of graphene and a dielectric. The transfer matrix method gives the possibility to relate the amplitudes of the incident and reflected electromagnetic waves at the input to the layered structure with the amplitudes at the output by means of propagation and transfer matrixes. The frequency dependent optical conductivity of graphene sheet is calculated by Kubo formula which takes into account both interband and intraband transitions. It is shown that when the chemical potential of graphene is increased, the elliptic form of the dispersion curve turns into to hyperbolic. This result is due to the fact that the perpendicular component of the permittivity changes its sign when the chemical potential is changed.
Key words: hyperbolic metamaterials, graphene, dispersion of electromagnetic waves.

Introduction

Strongly anisotropic media, in which the components of the diagonal tensor of permittivity or permeability have opposite signs, are called hyperbolic media or hyperbolic metamaterials (HMM) [1]. These materials are of great practical interest associated not only with the comparative ease of their fabrication, but mostly with their unusual optical properties. It is known that the hyperbolic metamaterials, along with the negative refraction of light [2], can be used to overcome the diffraction limit [3-6], to realize optical resonators and waveguides at the nanoscale [7,8], to develop biosensor applications [9] and to enhance nonlinear effects [10]. In most cases, the hyperbolic metamaterials are obtained on the basis of a composition of metal nanoparticles immersed into dielectric media. There are two main methods for obtaining materials with the hyperbolic dispersion. In the first case, the hyperbolic response is achieved due to alternating layers of metal and dielectric, and the second is due to metal nanowires, arranged in a dielectric medium.

At present, research is actively under way on the development of the hyperbolic materials based on a graphene. The graphene, which is a single layer of graphite, has very unique electrical, magnetic and thermal properties [11-13]. Electrons in the graphene behave like the photons in a vacuum, i.e. they have a zero effective mass, which leads to a linear dispersion law [14]. In addition, strong plasmon effects are observed in the graphene, which, if necessary, can be influenced by doping [12].

In this paper possibility of creating a medium based on graphene-dielectric (quartz) structures with a hyperbolic shape of the dispersion relation is considered (Figure 1).

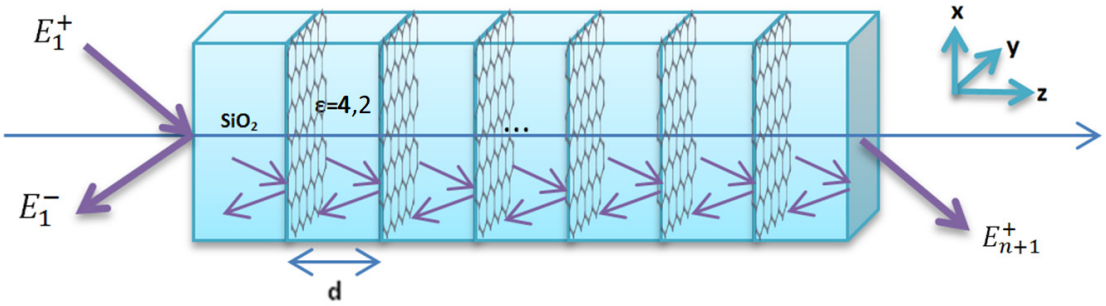

Figure 1 – Layout of layers of periodic structure based on dielectric and graphene

Optical conductivity of graphene

The electromagnetic properties of grapheme sheets are characterized by the surface conductivity σ within the Kubo formalism. In the absence of an external magnetic field, the surface conductivity of grapheme sheet is defined as a sum of the intraband and interband conductivities as:

$$\sigma=\sigma_{\text{intra}}+\sigma_{\text{inter}} \tag{1}$$

where

$$\sigma_{\text{intra}}=\frac{ie^2k_bT}{\pi\hbar^2(\omega+i2\gamma)}\left(\frac{\mu}{k_bT}+2\text{Log}\left[e^{-\frac{\mu}{k_bT}}+1\right]\right), \tag{2}$$

$$\sigma_{\text{inter}}=\frac{ie^2}{4\pi\hbar^2}\text{Log}[\frac{2\mu-(\omega+i2\gamma)\hbar}{2\mu+(\omega+i2\gamma)\hbar}]. \tag{3}$$

Here $\hbar$ denotes the Plank constant, μ is the chemical potential, γ refers to the electron-phonon scattering rate, ω designates the incident wave frequency, k_b stands for the Boltzmann constant, T signifies the temperature and e is simply the elementary charge.

Figure 2 displays the imaginary and real parts of the surface conductivity, which is normalized to $\sigma_0=\frac{e^2}{4\hbar}$.

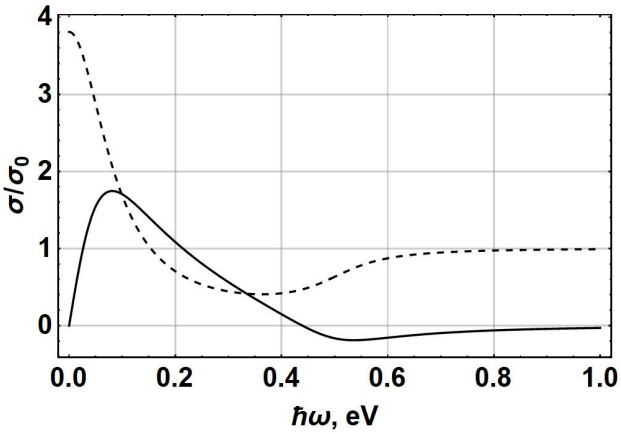

$\mu=0.25$ eV, $T=300$ K, $\Gamma=0.043$ eV

Figure 2 – Optical conductivity of the graphene sheet. Solid line: the imaginary part; dashed line: the real part.

The matrix method or the matrix transfer method makes it possible to relate the amplitudes of the incident and reflected electromagnetic waves at the input to the layered structure with the amplitudes at the output by means of the matrix M

$$\begin{bmatrix}E_1^+\\E_1^-\end{bmatrix}=M\begin{bmatrix}E_{n+1}^+\\E_{n+1}^-\end{bmatrix}, \tag{4}$$

which is obtained by multiplying: the transition matrix T through the interface, and the transmission matrix in a dielectric medium P_d :

$$M_{TM}=T\cdot P_d=\begin{bmatrix}1+\zeta_{TM}/2 & \zeta_{TM}/2\\ \zeta_{TM}/2 & 1-\zeta_{TM}/2\end{bmatrix}\begin{bmatrix}e^{-ik_zd} & 0\\0 & e^{ik_zd}\end{bmatrix}. \tag{5}$$

Here $\zeta_{TM}=\sigma(\omega,\mu,\Gamma,T)k_z/\varepsilon\varepsilon_0\omega$ stands for the so-called wave impedance, $\sigma(\omega,\mu,\Gamma)$ denotes the conductivity of graphene, determined by the Kubo formula (1). Note that a wave is considered to be polarized parallel to the graphene sheet at the interface, since it is for this wave that the hyperbolic dependence of its dielectric properties is observed.

To find the dispersion relation, we consider a wave propagating in the direction of the z axis. This wave is weakened due to passing through each layer of the dielectric, so that in each layer of an infinite periodic structure the following conditions hold

$$E_{n+1}^+=E_n^+e^{-\alpha d}, \tag{6}$$

$$E_{n+1}^-=E_n^-e^{-\alpha d}. \tag{7}$$

Solving equations (6) - (7) together with (4), it is not difficult to obtain the following homogeneous equation in the matrix form

$$\begin{pmatrix}M_{11}-e^{\alpha d} & M_{12}\\ M_{21} & M_{22}-e^{\alpha d}\end{pmatrix}\begin{pmatrix}E_{n+1}^+\\E_{n+1}^-\end{pmatrix}=0, \tag{8}$$

whose nonzero solution only exists if the determinant of the matrix turns zero

$$M_{11}M_{22}+e^{2\alpha d}-(M_{11}+M_{22})e^{\alpha d}-M_{12}M_{21}=0. \tag{9}$$

Here, α is the Bloch wave number, d designates the thickness of the dielectric gap.

Recalling that the condition $M_{11}M_{22} - M_{12}M_{21} = 1$ must always be satisfied for a periodic structure, expression (9) is simplified to the following form:

$$\mathrm{Cosh}(\alpha d) = (M_{11} + M_{22})/2. \qquad (9)$$

If α is considered a complex number $\alpha = \beta + i\kappa$, at which $\mathrm{Cosh}(\alpha d) = \mathrm{Cosh}(\beta d)\mathrm{Cos}(\kappa d) + i\,\mathrm{Sinh}(\beta d)\mathrm{Sin}(\kappa d)$, then, two limiting cases arise. Of interest is only the first case that corresponds to an undamped wave in the periodic structure and strictly determines its bandwidth

$$\mathrm{Cos}(\kappa d) = \frac{M_{11} + M_{22}}{2} = \\ = \mathrm{Cos}(k_z d) - i\frac{\zeta_{TM}}{2}\mathrm{Sin}(k_z d) \qquad (10)$$

The dispersion relation (10) describes the law of propagation of a TM polarized wave in a periodic photon structure. It should be noted that in the subwave regime, at which $k_z d \ll 1$ and $\beta d \ll 1$, expression (10) turns into the dispersion relation obtained on the basis of the effective medium model:

$$\kappa^2 = \varepsilon_t k_0^2 - \frac{\varepsilon_t}{\varepsilon} k_\perp^2, \qquad (11)$$

where $\varepsilon_t = \varepsilon - i\sigma(\omega, \mu, \Gamma, T)/\varepsilon_0 \omega d$ denotes the perpendicular component of the permittivity.

Figure 3 shows the dependence of $\kappa = \kappa' + i\kappa''$ on the transverse component of the wave number $k_\perp$, normalized to k_0. For numerical calculations quartz SiO_2 with the permittivity of $\varepsilon = 4.2$ and the width of 80 nm has been chosen as a dielectric medium. It is clearly seen from the figure that for the small value of the dimensionless chemical potential $\mu = 0.1$, the dependence $\kappa(k_\perp)$ is purely elliptic, see Figure 3a, and the transition point of the curve corresponds to the value $\sqrt{\varepsilon}$. At $\mu = 0.6$ the elliptic character of the curve goes over to the hyperbolic, see Figure 3b. Note that, in practice, an increase in the chemical potential is merely achieved by doping of the graphene or by applying an external electric field.

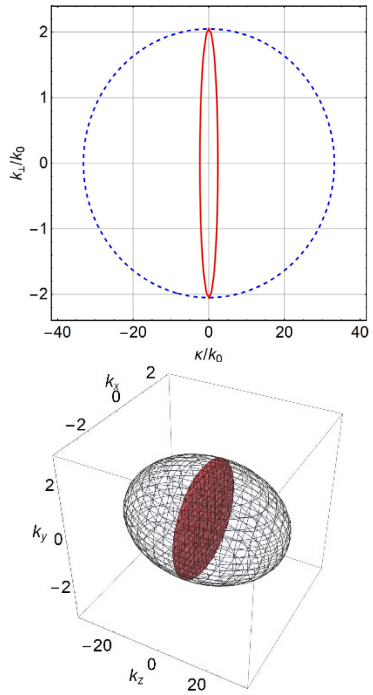

$\mu = 0.1$ eV, $T = 300$ K, $\hbar\omega = 0.91$ eV, $\Gamma = 0.043$ eV

a) Elliptic behavior of the dispersion

b)

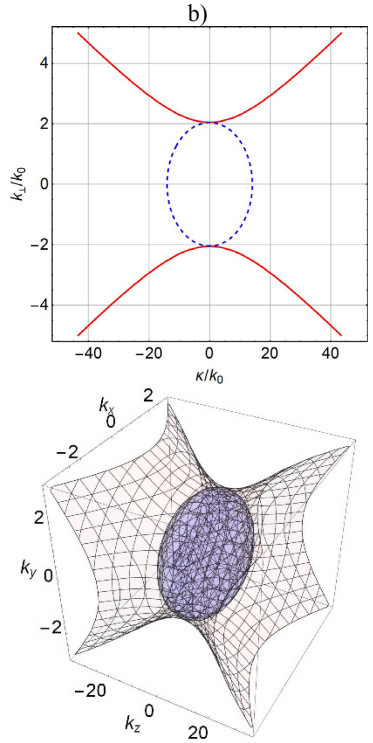

$\mu = 0.6$ eV, $T = 300$ K, $\hbar\omega = 0.91$ eV, $\Gamma = 0.043$ eV

b) Hyperbolic behavior of the dispersion

Figure 3 – Dependence of κ on $k_\perp = \sqrt{k_x^2 + k_y^2}$ at different values of the chemical potential

Conclusion

It is inferred from the figures above that when an external electric field, applied to graphene, is rather small such that the chemical potential μ is also not large, the dispersion law has purely elliptic shape. At the value of $\mu = 0.6$, a transition of the dispersion law is revealed, which manifests itself in the appearance of forbidden bands for a plane-polarized TM wave. In the frequency range, corresponding to the forbidden bands, the wave is completely reflected from the layered structure, whereas the transmitted wave has a minimum intensity. Based on the results obtained, it can be concluded that the graphene, due to its unique optical properties, is a more promising material for creating hyperbolic metamaterials than conventional metals. This statement is based on the fact that it is possible to control the light transmission through a layered structure by changing the chemical potential μ.

Reference

1 P. Shekhar., J. Atkinson., Z. Jacob. Hyperbolic metamaterials: fundamentals and applications //Nano Convergence. – 2014. – Vol. 1. – P. 14.

2 V.A. Podolskiy., Alekseyev L., E.E. Narimanov. Strongly anisotropic media: the THz perspectives of left-handed materials // Journal of Modern Optics. – 2005. – Vol. 52. – P. 2343-2349.

3 Z. Jacob., L.V. Alekseyev., E. Narimanov. Optical hyperlens: Far-field imaging beyond the diffraction limit // Optics Express. – 2006. – Vol. 14. – P. 8247-8256.

4 Z. Liu., S. Durant., H. Lee., Y. Pikus., N. Fang., Y. Xiong., C. Sun., X. Zhang. Far-field optical superlens // Nano letters. – 2007. – Vol. 7. – P. 403-408.

5 Z. Liu., H. Lee., Y. Xiong., C. Sun., X. Zhang. Far-field optical hyperlens magnifying sub-diffraction-limited objects // Science. – 2007. – Vol. 315. – P. 1686-1686.

6 I.I. Smolyaninov., Y.J. Hung., C.C. Davis. Magnifying superlens in the visible frequency range // Science. – 2007. – Vol. 315. – P. 1699-01701.

7 J. Yao., X. Yang., X. Yin., G. Bartal., X. Zhang. Three-dimensional nanometer-scale optical cavities of indefinite medium // Proceedings of the National Academy of Sciences. – 2011. – Vol. 108. – P. 11327-11331.

8 V.A. Podolskiy., E.E. Narimanov. Strongly anisotropic waveguide as a nonmagnetic left-handed system // Physical Review B. – 2005. – Vol. 71. – P. 201101.

9 A.V. Kabashin., P. Evans., S. Pastkovsky., W. Hendren., G.A. Wurtz., R. Atkinson., R. Pollard., V.A. Podolskiy., A.V. Zayats. Plasmonic nanorod metamaterials for biosensing // Nature materials. – 2009. – Vol. 8. – P. 867-871.

10 G.A. Wurtz., R. Pollard., W. Hendren., G.P. Wiederrecht., D.J. Gosztola., V.A. Podolskiy., A.V. Zayats. Designed ultrafast optical nonlinearity in a plasmonic nanorod metamaterial enhanced by nonlocality // Nature nanotechnology. – 2011. – Vol. 6. – P. 107-111.

11 A. K. Geim., K. S. Novoselov. The rise of graphene // Nature materials. – 2007. – Vol. 6. – P. 183-191.

12 L. Ju., B. Geng., J. Horng., C. Girit., M. Martin., Z. Hao., H. A. Bechtel. Graphene plasmonics for tunable terahertz metamaterials // Nature nanotechnology – 2011. – Vol. 6. – P. 630-634.

13. B. Francesco., Z. Sun. T., Hasan., A. C. Ferrari. Graphene photonics and optoelectronics // Nature photonics. – 2010. – Vol. 4. – P. 611-622.

14. K. S. A. Novoselov. et al. Two-dimensional gas of massless Dirac fermions in graphene // Nature. – 2005. – Vol. 438. – P.197-200.

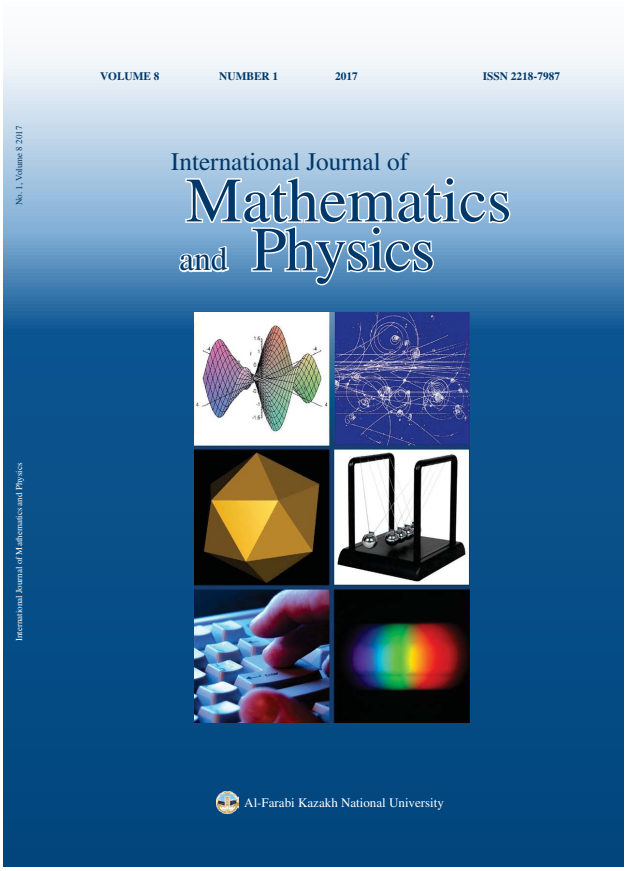

International Journal of Mathematics and Physics

One of the main goals of the Journal is to promote extensive exchange of information between scientists from all over the world. We propose publishing services for original papers in Mathematics and Physics and also for conference proceedings held in the Republic of Kazakhstan and abroad.

The Journal publishes experimental and theoretical research works in Mathematics, Mathematical physics, Physics andApplied Physics. Particularly the following sectionsare considered: Modern problems of Calculus Mathematics, Algebra and Mathematical Analysis, Differential Equations and Mechanics, Informatics and Mathematical Modeling, Calculus of Approximations and Program Systems, Astronomy and Space Research, Theoretical Physics and Plasma Physics, Chemical Physics and Radio Physics, Thermophysics, Nuclear Physics and Nanotechnology.

The International Journal of Mathematics and Physics is apeer-reviewed journal published by al-Farabi Kazakh National Universitytwo times a year. We hope to receive papers from research laboratories which are interested in sharing their ideas among their colleagues on scientific principles of mathematical and physics, and are carrying out researchers on such subjects as production of new material or technological problems.

The journal “International Journal of “Mathematics and Physics” was registered by the Ministry of Culture, Information and Public Accord of the Republic of Kazakhstan. The ISSN is 2218-7987.

The journal website http://ijmph.kaznu.kz provides free access to full-text articles published since 2010.